Eur. Phys. J. B **20**, 35–54 (2001)

THE EUROPEAN
PHYSICAL JOURNAL B
EDP Sciences

Magnetic anisotropy and domain patterns in electrodeposited cobalt nanowires

Y. Henry[1,a], K. Ounadjela[1], L. Piraux[2], S. Dubois[3], J.-M. George[4], and J.-L. Duvail[5]

[1] Institut de Physique et Chimie des Matériaux de Strasbourg[b] and Université Louis Pasteur, 23 rue du Loess, 67037 Strasbourg Cedex, France
[2] Département des Sciences des Matériaux et des Procédés, Université Catholique de Louvain, Place Croix du Sud 1, Louvain la Neuve 1348, Belgium
[3] Laboratoire de Métallurgie Physique[c] and Université de Poitiers, 86960 Futuroscope Cedex, France
[4] Laboratoire Central de Recherches Thomson[d], Domaine de Corbeville, 91404 Orsay, France
[5] Institut des Matériaux de Nantes[e] and Université de Nantes, 2 rue de la Houssinière, 44322 Nantes Cedex 03, France

Received 14 September 2000

Abstract. The magnetic anisotropy and domain structure of electrodeposited cylindrical Co nanowires with length of 10 or 20 μm and diameters ranging from 30 to 450 nm are studied by means of magnetization and magnetic torque measurements, as well as magnetic force microscopy. Experimental results reveal that crystal anisotropy either concurs with shape anisotropy in maintaining the Co magnetization aligned along the wire or favours an orientation of the magnetization perpendicular to the wire, hence competing with shape anisotropy, depending on whether the diameter of the wires is smaller or larger than a critical diameter of 50 nm. This change of crystal anisotropy, originating in changes in the crystallographic structure of Co, is naturally found to strongly modify the zero (or small) field magnetic domain structure in the nanowires. Except for nanowires with parallel-to-wire crystal anisotropy (very small diameters) where single-domain behaviour may occur, the formation of magnetic domains is required to explain the experimental observations. The geometrical restriction imposed on the magnetization by the small lateral size of the wires proves to play an important role in the domain structures formed.

PACS. 75.50.-y Studies of specific magnetic materials – 75.30.Gw Magnetic anisotropy – 75.60.Ch Domain walls and domain structure

1 Introduction

In response to the ever-increasing demands for high performance data storage media and sensing devices, great effort is currently put into the development and studies of innovative magnetic materials. Most magnetic devices marketed nowadays still use bulk or thin film materials. This is soon to change with the advent of nanofabrication technologies. Nanofabrication offers the technical ability to fabricate magnetic objects with nanometric scale precision having unique magnetic properties, which may be tailored by manipulating the size, the shape, or the composition of the nanostructures. Many of these properties come about by imposing a geometrical restriction on the magnetization. As the size of the nanomagnets becomes comparable to key magnetic length scales, such as the exchange length (in the nm range) or the domain wall width (nm–μm range), the magnetization configuration may indeed be strongly affected. The understanding of how finite lateral size may affect the magnetic behaviour of nanostructures is of primary importance from practical and theoretical viewpoints. Several techniques may be employed to investigate the magnetic properties of nanostructures. Among them, microSQUID's [1], magnetoresistance measurements [2–4], electron Lorentz microscopy [5] or holography [6], and magnetic force microscopy [7–9] have proved to be valuable tools in studying single nanoelements.

Necessary to achieve ultra-high density in magnetic storage media is that the lateral size of the information bits be as small as possible, without though the bit volume reaches the superparamagnetic limit beyond which the energy needed to switch the magnetization of a bit becomes less than the thermal energy. Also required is that the transition region between two bits of opposite magnetization be as narrow as possible, which in continuous thin film media is clearly hindered by the finite width of the domain walls. A promising way to achieve small lateral size, with comparatively large volume and hence high magnetic anisotropy energy of the bits is to realise arrays

---

[a] e-mail: `yves.henry@ipcms.u-strasbg.fr`
[b] CNRS UMR 7504
[c] CNRS UMR 6630
[d] CNRS/Thomson-CSF UMR 137
[e] CNRS UMR 6502

of nanometric magnetic pillars [10]. This allows to remove the limitations listed before as each bit then consists of a single-domain element, not experiencing exchange interactions with its neighbours however close they are, and having two well defined magnetization states of equal magnitudes and opposite directions determined by the strong shape anisotropy of the element.

Advanced lithographic techniques are currently employed to make regular periodic arrays of submicronic magnetic wires, dots and pillars. As an alternative, electrochemical deposition of ferromagnetic metals into porous templates is performed to produce arrays of nanopillars (or nanowires). The most commonly used templates are polycarbonate membranes [11–13]. Although, at present, nanowires cannot be grown at prespecified locations in such templates, which is required for magnetic storage applications, this technique has the attractive features of extreme simplicity in operation and high cost-effectiveness.

In this paper, the magnetic anisotropy properties and the magnetic domain patterns in 10 or 20 μm long electrodeposited Co wires with diameters ranging from 30 to 450 nm are studied by means of magnetization and magnetic torque measurements as well as magnetic force microscopy (MFM). Experimental results reveal that shape and crystal magnetic anisotropies either compete with each other or add to each other depending on whether the diameter of the Co wires is larger or smaller than a critical diameter of 50 nm. This change in anisotropy properties, driven by changes in crystallographic structure, is found to strongly modify the zero (or small) field magnetic domain structure within the Co nanowires. Except for nanowires with very small diameters where single-domain behaviour may occur, magnetic domain formation is required to explain the experimental observations.

2 Nanowire fabrication and experimental procedures

Random arrays of nanowires were made by electrodeposition of Co in the pores of home-made high-quality track-etched polycarbonate membranes. The membranes were first irradiated with Ar^{9+} ions accelerated at 120 MeV and subsequently etched chemically [14]. The irradiation was performed at normal beam incidence with respect to the plane of the polycarbonate films and the dispersion in the direction of the ion tracks was less than 10 degrees. The etching conditions were adapted to produce regular cylindrical pores of varying diameters. A thin metal film of Au, Ag or Cu was then deposited by thermal evaporation on one side of the porous membranes to be filled to serve as a cathode. The growth was performed by electrodeposition at room temperature from a sulfate bath containing Co^{2+} ions under potentiostatic control using a conventional three-electrodes cell. Boric acid was introduced in the plating bath so as to reduce the local increase of pH in the vicinity of the cathode, owing to its buffering action [15]. The deposition potential was -0.9 V while the pH in the bulk of the bath was typically 3.8. The filling of the pores was monitored by measuring the plating current. The deposition was stopped as soon as three-dimensional caps began to form on top of the few first emerging wires, which was revealed by a sudden increase of plating current. Using this growth procedure, similar to the one described by Withney *et al.* [12], well-defined straight wires were produced, whose length equals the membrane thickness (10 or 20 μm) and which have relatively small surface roughness, almost uniform circular cross section all along the wire length and narrow diameter distribution (Fig. 1).

Fig. 1. Electrodeposited Co nanowires observed with high performance scanning electron microscopy after dissolution of the polycarbonate membrane in dichloromethane. The average wire diameter is 90 nm.

For this study, we used polycarbonate membranes with low porosity. The average spacing between the pores is larger than 1 μm so that the dipolar interactions between the magnetic elements contained in the pores are certainly small [16]. As a consequence, the magnetic properties of the arrays of nanowires are expected to be similar to those of assemblies of isolated objects. In order to keep the initial parallel alignment of the wires and take advantage of it, all of the macroscopic magnetic measurements were performed first, on large assemblies of wires while still located inside the membranes. As for the local investigations by MFM, they were carried out on single wires after dissolving the polycarbonate templates in a dichloromethane solution and collecting the magnetic elements on clean and flat silicon substrates.

3 Coercivity and remanent magnetization

The magnetic properties of the Co nanowires were first studied by means of magnetization measurements carried out at room temperature using an alternating gradient force magnetometer (AGFM) (Fig. 2). The variation of the longitudinal coercive field (Fig. 3a) and remanent magnetization (Fig. 3b) as a function of the wire diameter ϕ was determined from such measurements with the external field applied along the wires (perpendicular to the membrane). In comparison with bulk Co which exhibits coercive fields of a few tens of oersteds (depending on the material microstructure), Co nanowires show greatly enhanced coercivities, as already observed by Whitney

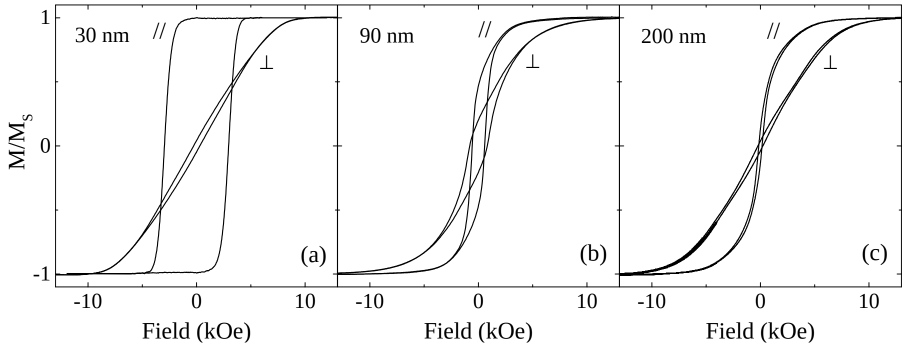

Fig. 2. Room temperature hysteresis loops measured on arrays of Co nanowires with the magnetic field applied parallel (||) and perpendicular ($\perp$) to the wire axis. The nanowires have average diameters of (a) 30 nm, (b) 90 nm and (c) 200 nm.

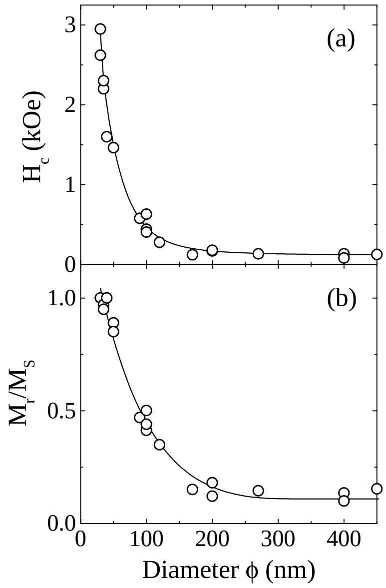

Fig. 3. Variation of the longitudinal coercivity (a) and squareness (b) with the average diameter of the Co nanowires. The lines are guides for the eye.

and co-workers [12]. In this respect, they behave in the same way as most ultrafine ferromagnetic particles which have a tendency to form magnetic single-domain structures. The enhancement of coercivity decreases rapidly as the wire diameter increases (Fig. 3a). This is expected since a larger diameter facilitates the formation of magnetic multi-domain structures, hence degrading the coercivity. The longitudinal squareness M_r/M_s diminishes also rapidly with increasing diameter, from a value close to 1 for the smallest diameter investigated, that is 30 nm, to 0.1 for diameters larger than 200 nm (Fig. 3b). This evolution is more intriguing.

For infinite homogeneously magnetized cylinders, the demagnetizing factors are respectively $N_\parallel = 0$ and $N_\perp = 2\pi$ for magnetic fields applied along directions respectively parallel and perpendicular to the revolution axis. Therefore, the shape anisotropy whose strength is $\frac{1}{2}(N_\perp - N_\parallel)M_s^2 = \pi M_s^2$ tends to maintain the magnetization of a cylindrical wire aligned along its revolution axis. For wires with pure shape anisotropy, an external field of at least $2\pi M_s$ (8.8 kOe for Co) is required to fully orient the magnetization perpendicular to the revolution axis and square hysteresis loops should be recorded when the external field is applied along the axial direction.

Despite the very high length to diameter ratio hence the strong shape anisotropy of the Co nanowires, square longitudinal hysteresis loops are only observed for diameters smaller than 50 nm. This result as well as the decrease of the longitudinal remanence with increasing diameter can be understood in the light of results from X-ray diffraction (XRD) and transmission electron microscopy (TEM) experiments, a brief summary of which follows. First, Co nanowires were shown to be made of large crystal grains extending transversally across the full wire diameter and longitudinally over several micrometers. Second and more important, electrodeposited Co proved to adopt a rather good quality hexagonal compact structure with a preferential texture which depends on the diameter of the wires. For diameters smaller than $\phi_{\rm crit} \simeq 50$ nm, the c-axis is preferentially oriented parallel to the revolution axis of the wires (Fig. 4a, b), whereas for diameters larger than $\phi_{\rm crit} \simeq 50$ nm it is aligned within 10° of the normal to the wire axis (Fig. 4c), as was also shown by Maurice *et al.* [17]. Cobalt wires should thus possess a strong crystal anisotropy ($K_1 = 5.3 \times 10^6$ erg/cm^3 in bulk *hcp* Co [18]), almost similar in size to the shape anisotropy ($\pi M_s^2 = 6.2 \times 10^6$ erg/cm^3 with $M_s = 1400$ emu/cm^3) and always favouring an alignment of the magnetization along the c-axis. Therefore, crystal anisotropy should be found to either compete or collaborate with shape anisotropy depending on whether the diameter of the Co wires is larger or smaller than $\phi_{\rm crit} \simeq 50$ nm. Although the revolution axis seems to remain the easiest direction of magnetization whatever the diameter ϕ (Fig. 2), its easy character is reduced for large ϕ, because of the competition suggested just before. This competition that will be ascertained later in this paper by magnetic torque measurements (Sect. 4.1) is at the origin of the formation of magnetic domains with partial or full transverse orientation when reducing the longitudinally applied field (Sects. 4.2 and 5.2.2). It thus explains the drop in longitudinal remanent magnetization observed when increasing the diameter of the Co nanowires [16]. It also accounts for what may appear as

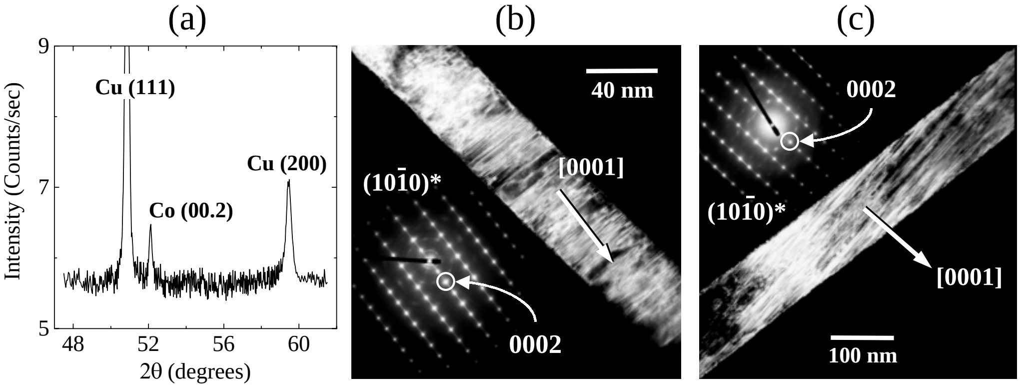

Fig. 4. (a) $\theta/2\theta$ XRD spectrum recorded on an array of Co nanowires, 35 nm in nominal diameter, with the diffraction vector parallel to the wires ($\lambda = 0.1789$ nm). Co possesses its normal equilibrium *hcp* phase with a strongly dominating [0001] texture (c-axis parallel to the wire). From the position of the (0002) diffraction peak ($2\theta = 52.13°$) one deduces a lattice parameter $c = 0.4072$ nm, very close to the bulk value of 0.4069 nm. Note also the presence of two diffraction peaks associated with the Cu film which served as a cathode during electrodeposition. (b, c) Dark field TEM images showing the preferred orientation of the close-packed planes: (b) Almost perpendicular to the wire axis ($\mathbf{c} \parallel$ wire) in Co nanowires with small diameters, (c) almost parallel to the wire axis ($\mathbf{c} \perp$ wire) in Co nanowires with large diameters. Insets: Selected area diffraction patterns corresponding to the micrographs ($\langle 10\bar{1}0\rangle$ zone axis). The long streaks in the [0001] direction indicate the presence of *fcc*-like stacking faults.

an anomaly, namely the fact that for large diameters the coercivity of the nanowires is maximum for an applied field perpendicular to the wires (Fig. 2b, c).

4 Magnetic anisotropy

4.1 High field magnetic torque measurements

High field magnetic torque measurements were carried out as a function of wire diameter and temperature in order to determine accurate values for the Co crystal anisotropy as well as the direction of the associated easy and hard axes and thus ultimately confirm the changes of texture and crystal anisotropy in the Co nanowires mentioned previously (Sect. 3). Preliminary experiments performed by rotating the external magnetic field in the plane perpendicular to the wires (membrane plane) showed no anisotropy of the torque for assemblies of several hundred thousands of Co elements, whatever their diameter. This result reveals that, when perpendicular to the revolution axis, the [0001] directions of the Co cylindrical crystals located inside the membranes are randomly oriented in the plane perpendicular to the wires.

The high field torque curves whose analysis is presented in the following (Fig. 5a, b) were recorded as the applied magnetic field $\mathbf{H}$ was rotated in a plane containing the revolution axes of the nanowires. The external field of $H = 12$ kOe was large enough to saturate the magnetic moment of the sample $\boldsymbol{\mu}$, hence insuring a single-domain state in the magnetic cylinders. The experimental curves consist of the variation of the anisotropy torque Γ_a as a function of the applied field angle θ_H. Hence, they suffer from a shear-distortion resulting from the slight angle-dependent misalignment of the magnetic moment $\boldsymbol{\mu}$ (angle θ) and applied field which writes $(\theta - \theta_H) = \arcsin(\Gamma_\mathrm{a}/\mu H)$ [19]. For all diameters and temperatures investigated, the experimental data were closely fitted after the torque curves were sheared in proportion to their ordinate by $\arcsin(\Gamma_\mathrm{a}/\mu H)$, *i.e.* corrected adequately for the misalignment of the magnetization and applied field. The anisotropy energy that was considered for the fits is

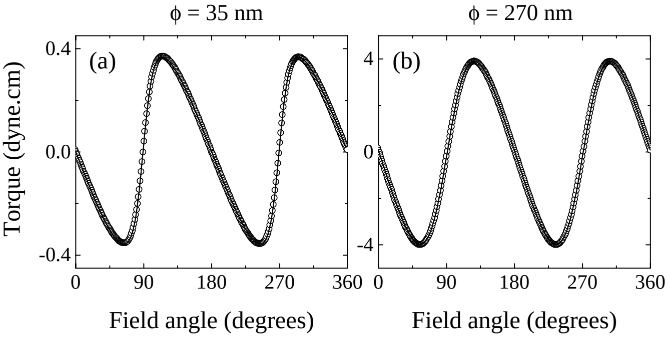

Fig. 5. High field torque curves measured at room temperature on arrays of Co nanowires with average diameters of (a) 35 nm and (b) 270 nm (open circles) and fits to the experimental data according to equation 2 (solid line). The curves were recorded as the applied field was rotated in a plane parallel to the wire axis, the field angle being measured from the direction of the wire axis.

$$E_\mathrm{a}(\theta) = K_1^\mathrm{eff}\sin^2\theta + K_2\sin^4\theta \qquad (1)$$

which corresponds to a magnetic anisotropy torque of the form

$$\Gamma_\mathrm{a}(\theta) = -\frac{\partial E_\mathrm{a}(\theta)}{\partial\theta} = -(K_1^\mathrm{eff} + K_2)\sin(2\theta) + \frac{K_2}{2}\sin(4\theta) \qquad (2)$$

where θ is the angle between the direction of the magnetization of the wires and the direction of their revolution

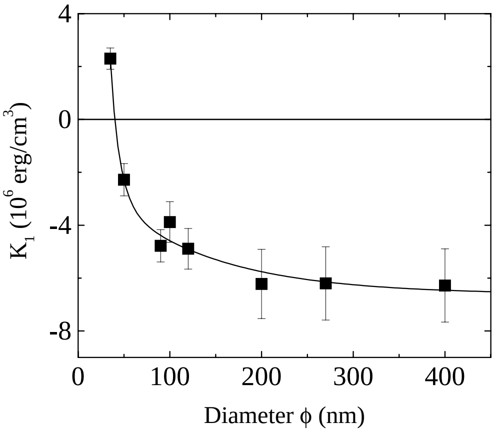

Fig. 6. Variation of the first order crystal anisotropy constant K_1 with the average diameter of the Co nanowires. The solid line is a guide for the eye.

axes (normal to the membrane), K_1^{eff} is an effective first order uniaxial anisotropy constant supposedly containing shape (πM_s^2) and crystal (K_1) contributions and K_2 is a second order uniaxial anisotropy constant. Although it had to be considered to achieve very good fits of the experimental data, K_2 was for most diameters found negligible as compared to the effective first order uniaxial anisotropy (K_1^{eff}).

4.1.1 Anisotropy versus diameter

The room temperature variation of the first order crystal anisotropy (K_1) as a function of the wire diameter is shown in Figure 6. The rather large error bars are mainly due to uncertainty in the volume of magnetic material contained in the pores of the membranes. Note that for diameters larger than $\phi_{\mathrm{crit}} \simeq 50$ nm the K_1 values deduced from the experimentally measured K_1^{eff}'s by subtracting πM_s^2 were multiplied by a factor of 2 to account for the random orientation of the *c*-axis in the plane perpendicular to the wires (see before). As expected from the change of texture in the Co nanowires revealed by the structural characterisation, the sign of K_1 changes when the diameter exceeds $\phi_{\mathrm{crit}} \simeq 50$ nm. Below ϕ_{crit} ($\phi = 35$ nm), K_1 is positive. According to equation (1), this means that crystal anisotropy collaborates with shape anisotropy in maintaining the magnetization aligned along the revolution axis of the wires. Above $\phi_{\mathrm{crit}} \simeq 50$ nm, K_1 is negative. Thus, crystal anisotropy tends to align the Co magnetization perpendicular to the wires and competes with shape anisotropy. However, crystal anisotropy never overcomes shape anisotropy ($\pi M_s^2 + K_1$ is always positive at room temperature) so that the revolution axis remains for all diameters the easiest direction of magnetization in the single-domain wires. Finally, the fact that K_1 varies in a continuous manner with ϕ and reaches values close to the one reported for bulk Co ($K_1 = 5.3 \times 10^6$ erg/cm^3 after Ref. [18]) only for those diameters which are larger than 100 nm indicates that the change of Co texture is probably progressive rather than abrupt, taking place in some but not in all wires or in some parts but not everywhere in the wires having medium diameters.

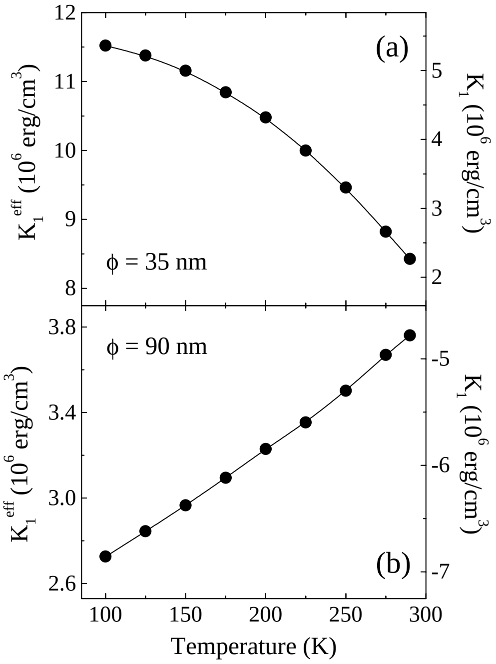

Fig. 7. Variation of the effective first order anisotropy constant K_1^{eff} with temperature for arrays of Co nanowires with nominal diameters of (a) 35 nm and (b) 90 nm.

4.1.2 Anisotropy versus temperature

Low temperature torque measurements were taken on two arrays of nanowires with diameters respectively smaller ($\phi = 35$ nm) and larger ($\phi = 90$ nm) than the critical diameter of $\phi_{\mathrm{crit}} \simeq 50$ nm. These experiments reveal opposite thermal behaviours for the effective first order uniaxial anisotropy constants K_1^{eff} of the two assemblies (Fig. 7). This is an immediate consequence of the change of sign of the first order crystal anisotropy constant (K_1) that accompanies the change of texture preferentially adopted by Co, as we shall explain now. In good approximation, shape anisotropy is identical for the two wire diameters (very large length to diameter ratio for the two samples) and does not vary significantly in the temperature range investigated (almost constant M_s). For both diameters, the absolute value of K_1, as deduced from the K_1^{eff} constant determined experimentally assuming a temperature and diameter independent shape anisotropy of $\pi M_s^2 = 6.2 \times 10^6$ erg/cm^3, increases monotonously with decreasing temperature, in qualitative agreement with results on bulk *hcp* Co [18]. For ϕ smaller than ϕ_{crit}, crystal anisotropy reinforces shape anisotropy ($K_1 > 0$). Therefore, K_1^{eff} increases as the temperature decreases (Fig. 7a). On the contrary for ϕ larger than ϕ_{crit}, crystal anisotropy counteracts shape anisotropy ($K_1 < 0$). Hence, K_1^{eff} diminishes as the temperature is reduced (Fig. 7b).

4.2 Low field magnetic torque measurements

As we will show hereafter from results of torque measurements carried out with small applied magnetic fields, the change of Co crystal anisotropy demonstrated in the previous section induces a modification of the direction along which the residual magnetization of arrays of Co nanowires tends to align in zero or small magnetic fields. Notice that all torque experiments presented in the next discussion were performed respecting the following procedure. The magnetization of the investigated samples was first saturated with a large magnetic field applied perpendicular to the wires. Then, the strength of the field was reduced to the required value while its direction was unchanged. Finally, the external field was rotated in a plane parallel to the revolution axes of the nanowires and the torque curves were taken successively for both clockwise and counter-clockwise directions of rotation.

As is observed for most ferromagnetic materials, the torque curves recorded on the nanowires studied become hysteretic when one reduces the strength of the external field below the minimum intensity that is required to ensure a single-domain state and a fully reversible rotation of the magnetization as the applied field is rotated. Moreover, when doing so for Co electrodeposited wires, the torque curves obtained retain, over a certain range of magnetic field, the particular symmetry they exhibit in stronger field, when entirely reversible. Hence, in the case of the wires whose properties are analysed in this section, torque curves keep their uniaxial symmetry as rotational hysteresis starts to appear (Fig. 8a, b). However, if the external field is further reduced, the torque curves undergo a progressive change of shape (Fig. 8c, d) and end up at very low field with no significant rotational hysteresis and a symmetry that is no longer uniaxial but unidirectional (Fig. 8e, f). The occurrence of such reversible unidirectional torque curves proves that the residual magnetization of the nanowire arrays ($\mathbf{M}_\mathrm{r}$) does no longer follow the rotating external field ($\mathbf{H}$) but is rather frozen along a particular direction which is an easy direction of magnetization in small fields. The reason for this freezing is that the Zeeman torque exerted by the applied field on the residual magnetization is too weak to overcome the anisotropy energy barrier (note that the word freezing is not being used here in a literal sense since $\mathbf{M}_\mathrm{r}$ is not completely locked but rather oscillates slightly around the easy axis as the external field is rotated). To convince ourselves of this result, a simple model can be used, such as the one described later in this paper (last paragraph of Sect. 4.2).

A comparison between the torque curves recorded in the high and low magnetic field regimes defined before on samples with $\phi = 35$ nm (Fig. 8a, c, e) and $\phi = 90$ nm (Fig. 8b, d, f) shows once again that Co nanowires exhibit different magnetic behaviours depending on whether their diameter is larger or smaller than $\phi_\mathrm{crit} \simeq 50$ nm. More precisely, the phase shift of approximately 90 degrees observed between the unidirectional torque curves recorded on these wires (Fig. 8e, f) indicates that the direction along which the residual magnetization is pinned reorients as ϕ exceeds ϕ_crit. From the angles corresponding to the stable positions in the experimental torque curves, we can state that $\mathbf{M}_\mathrm{r}$ is parallel to the revolution axis of the wires for ϕ larger than ϕ_crit whereas it is perpendicular to this axis for ϕ smaller than ϕ_crit. In a single-domain picture, this latter statement is in contradiction with the fact that the overall uniaxial anisotropy $\pi M_\mathrm{s}^2 + K_1$ is always measured positive (at room temperature), implying a preference for a longitudinal orientation of the magnetization. Hence, the formation of magnetic domains must be invoked to account for this experimental result.

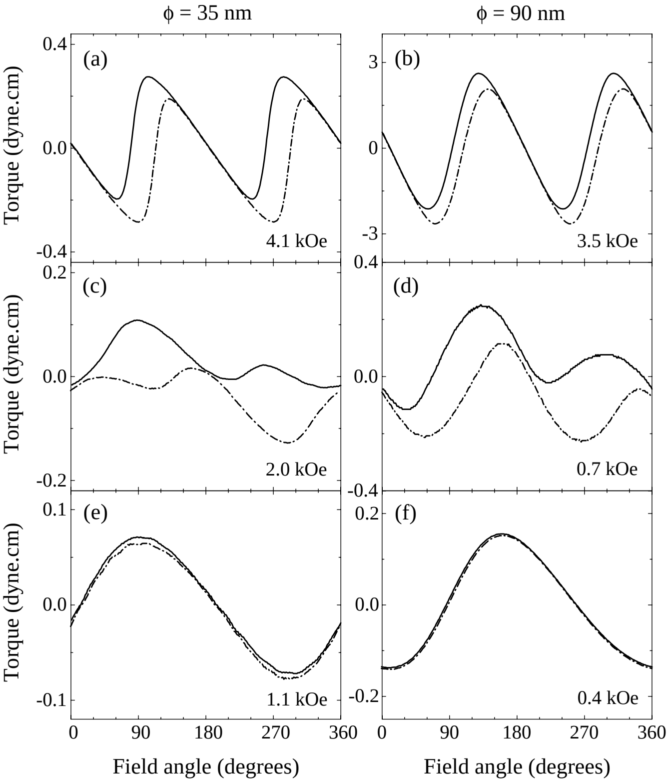

Fig. 8. Low field torque curves measured on arrays of Co nanowires with nominal diameters of (a, c, e) 35 nm and (b, d, f) 90 nm for decreasing values of the external field from top to bottom. Measurements were taken for both clockwise (solid line) and counter-clockwise (dashed line) directions of rotation of the applied field.

As mentioned previously, the magnetic behaviour of the Co nanowire arrays can, to a certain extent, be simulated using a very simple model, similar to the one developed by Stoner and Wohlfarth for describing magnetization reversals by coherent (or in unison) rotation of spins [20]. In this model, we consider a single magnetic moment $\boldsymbol{\mu}$ (magnetization $\mathbf{M}$) subjected only, besides the external field $\mathbf{H}$, to a first order uniaxial anisotropy of energy $K_\mathrm{u} \sin^2\theta$, θ being measured from the revolution axis of the wires. To briefly summarise, results from this model show that (i) rotational hysteresis occurs for field values ranging from $|K_\mathrm{u}|/M$ to $2|K_\mathrm{u}|/M$ and that (ii) a freezing of $\boldsymbol{\mu}$ along the easy axis of magnetization takes place for fields smaller than $|K_\mathrm{u}|/M$. Remarkably, a successful simulation of the unidirectional torque curves recorded

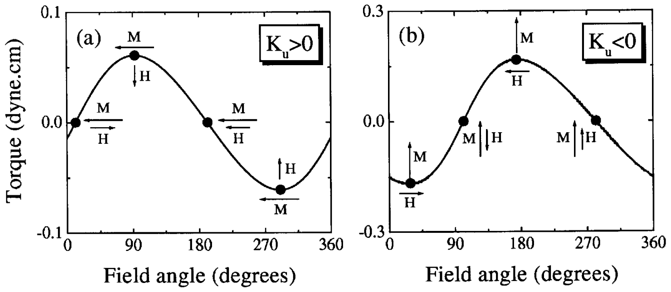

Fig. 9. Low field torque curves calculated from the model described in the text (Sect. 4.2), for (a) positive and (b) negative values of the uniaxial anisotropy constant K_u. Also depicted is the relative orientation of the rotating field **H** and magnetization **M** at particular points along these curves.

on the arrays of wires with $\phi = 35$ nm (Fig. 8e) and $\phi = 90$ nm (Fig. 8f) using this model requires to introduce K_u constants with the same signs as the K_1's measured for the two samples, *i.e.* positive (parallel-to-wire anisotropy) for $\phi = 35$ nm (Fig. 9a) and, more interesting, negative (perpendicular-to-wire anisotropy) for $\phi = 90$ nm (Fig. 9b). Then, in Co nanowires with diameters larger than ϕ_{crit}, the effective uniaxial anisotropy changes from positive in large fields to negative in small fields. This indicates that the dipolar contribution $\frac{1}{2}(N_\perp - N_\parallel)M_s^2$ to the total anisotropy energy diminishes upon reduction of the applied field so that crystal anisotropy becomes dominant, imposing the direction of $\mathbf{M}_r$ to be perpendicular to the wires axis. Such a diminution of dipolar energy can only occur through a change of demagnetizing factors ($N_\perp$, $N_\parallel$) following the formation of magnetic domains with partial or full transverse orientation, probably antiparallel to each other, so as to minimise simultaneously the dipolar and crystal energies.

5 Magnetic force microscopy

In the previous sections, we have clearly evidenced the correlation between the crystallographic structure and the magnetic properties of Co electrodeposited nanowires. The change of Co texture that occurs as the wire diameter ϕ exceeds $\phi_{\text{crit}} \simeq 50$ nm induces a strong modification of crystal anisotropy. Although the overall uniaxial anisotropy was always measured positive at room temperature, implying a preference for a longitudinal orientation of the magnetization in single-domain wires, a transverse orientation of the residual magnetization has been proved for arrays of wires with diameters larger than $\phi_{\text{crit}} \simeq 50$ nm. This result can only be understood if, due to the negative (perpendicular-to-wire) crystal anisotropy, magnetic domains with full or partial transverse orientation of the magnetization form at low field. In this section which is devoted to results from magnetic force microscopy experiments, the existence of such transversally magnetized domains will be ascertained.

In order to image the magnetic domains in the Co nanowires, a commercial Nanoscope III^{TM} AFM/MFM scanning probe microscope, equipped with a magnetically hard CoCr-coated tip magnetized along the tip axis, was used. We applied the popular tapping/lift^{TM} interlace technique developed by Digital Instruments. The particularities of this technique which are relevant for the interpretation of the observed magnetic contrasts are briefly described in Appendix A. Because of the proportionality of the recorded signal to the magnetic force derivative (see Appendix A), the technique employed provides a very good signal to noise ratio. However, it concomitantly makes the recovering of the local magnetic configuration within the sample not straightforward [21]. Indeed, modelling is most often required to ensure a correct interpretation of the observed MFM images. To evaluate theoretically the magnetic force exerted on the tip and its gradient, various levels of approximation are possible, depending on the degree of complexity of the model used to describe the shape and the magnetization state of both the tip and the sample [21]. The assumptions we made for the modelling of the MFM contrasts recorded on the nanowires are presented in Appendix B together with the analytical expressions that could be derived for the MFM response of longitudinally and transversally magnetized cylinders, upon which the modelling is based.

5.1 Nanowires topography

Sample shape is a key issue when interpreting the MFM images recorded on small objects with the tapping/lift^{TM} method. Indeed, the shape of the sample determines the trajectory of the magnetic probe (see Appendix A). Thereby, it determines the MFM signal measured so that a correct interpretation of the experimental MFM contrasts requires to take it into account. This point is clearly demonstrated in Appendix C. Therefore, great attention was paid to the sample topography. Assuming (as in the appendices) that the wires were lying parallel to the $\hat{\mathbf{x}}$ axis, the topographical profiles across the wires were fit to a reasonable accuracy using functions of the type

$$z = z_0 + \frac{H}{\left(\frac{y - y_c}{L}\right)^n + 1} \qquad (3)$$

which have already been used by Belliard and co-workers in their study of similar electrodeposited nanowires [9]. In this expression, z_0 is a vertical offset, H and $2L$ are respectively the height, the half-height width of the profile and y_c is the coordinate of the profile centre. Figure 10e is a summary of the relevant fit parameters obtained for typical topographical profiles taken on Co nanowires with nominal diameters of $\phi = 30$, 120, 200 and 450 nm (Fig. 10a–d). These first reveal that the height of the profiles are in all cases very close to, though most often slightly larger than the nominal wire diameter ϕ. This confirms our previous estimates of the wire diameters from scanning electron microscopy images. Second, they show that the half-height width of the profile $2L$ is always much larger than ϕ. We believe that two phenomena concur in enhancing the width of the topographical profiles across

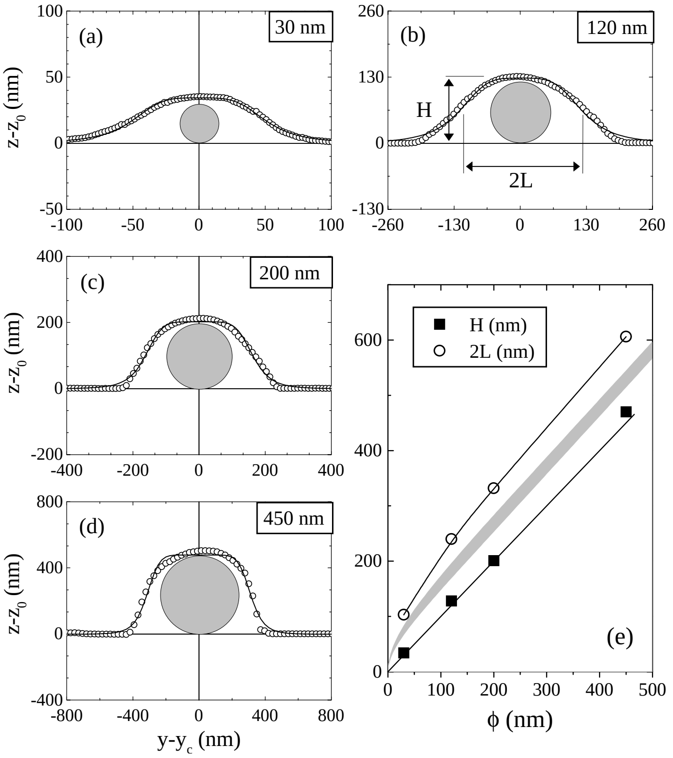

Fig. 10. (a–d) Typical topographical section profiles taken by AFM on Co nanowires with nominal diameters of 30, 120, 200 and 450 nm (open circle) and fits to the experimental data according to equation 3 (solid line). (e) Variation of the height H (solid square) and half-height full width $2L$ (open circle) of the AFM topographical profile with the nominal wire diameter ϕ. The shaded area delineates the $2L$ values expected for tip apex radii ranging between 30 and 50 nm (see Appendix D).

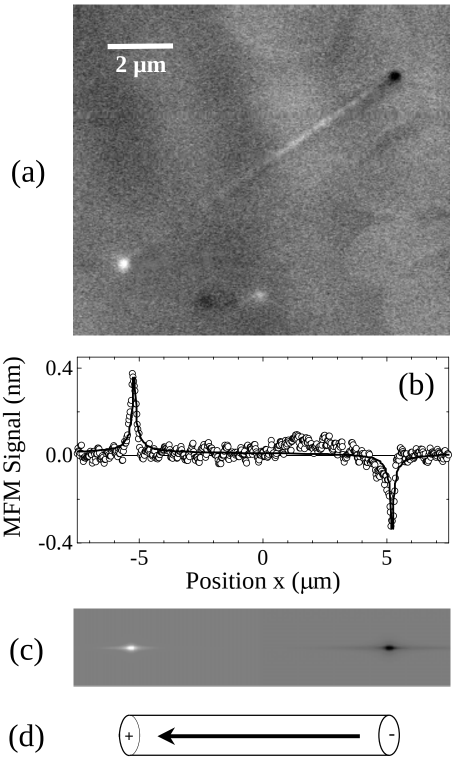

Fig. 11. (a) MFM image of a nominal 10 μm long, 35 nm thick Co nanowire after applying an axial field of 1.3 T (longitudinal remanent state). (b) Experimental (open circle) and theoretical (solid line) MFM profiles along the wire axis. (c) Simulated MFM contrasts assuming, as for the calculated profile shown in (b), the magnetic configuration sketched in (d), *i.e.* a homogeneous longitudinal magnetization in the wire.

the nanowires. The first one is the tip geometrical hindrance, described and modelled in Appendix D. The second one is that the polycarbonate/dichloromethane solution has been wetting the samples, leaving wide stripes of polymer on the flanks of the nanowires after evaporation of the solvent [9].

5.2 Magnetic domain structures

5.2.1 Nanowires with small diameters

Prior to MFM imaging, nanowires with diameters smaller than $\phi_{\rm crit} \simeq 50$ nm, *i.e.* nanowires where crystal anisotropy co-operates with shape anisotropy in maintaining the magnetization aligned along the revolution axis, were brought to their longitudinal or transverse remanent state by applying a strong magnetic field of 1.3 T in the adequate direction (respectively parallel and perpendicular to the wire axis). Let us first consider the case of a 35 nm thick, 10 μm long wire in the longitudinal remanent state such as shown in Figure 11a. The MFM image mainly consists of nearly complementary black and white contrasts spanning the ends of the cylinder (Fig. 11b). Contrary to these strong end-contrasts, the comparatively weaker (bright) contrast extending along part of the wire proved not to reverse upon reversal of the tip magnetization. It may then be safely ascribed to a still substantial topographical interaction between the sample and the tip, which is not inconsistent with the small lift height of 20 nm that was used for this experiment. A simulation based on equations (B.2) and (B.5), assuming an homogeneous longitudinal magnetization in the wire, leads to opposite MFM end-contrasts very similar to those observed experimentally (Fig. 11b, c). Thus, as sketched in Figure 11d, the small diameter wire in the longitudinal remanent state appears to behave as a single-domain axially magnetized cylindrical bar magnet with monopolar pole distributions located essentially on its circular end faces. This result is in perfect agreement with the longitudinal squareness $M_{\rm r}/M_{\rm s}$ of almost 1 measured on large assemblies of similar wires, while still embedded in polycarbonate membranes (Figs. 2a and 3b).

Let us now focus on a 10 μm long nanowire, 35 nm in nominal diameter, brought to the transverse remanent state such as shown in Figure 12a. This wire is not totally isolated since a 2 μm long fragment, apparently single-domain, has one of its extremities lying on top of the wire of interest. However, this fragment proved to have very little influence on the magnetic behaviour of the 10 μm long

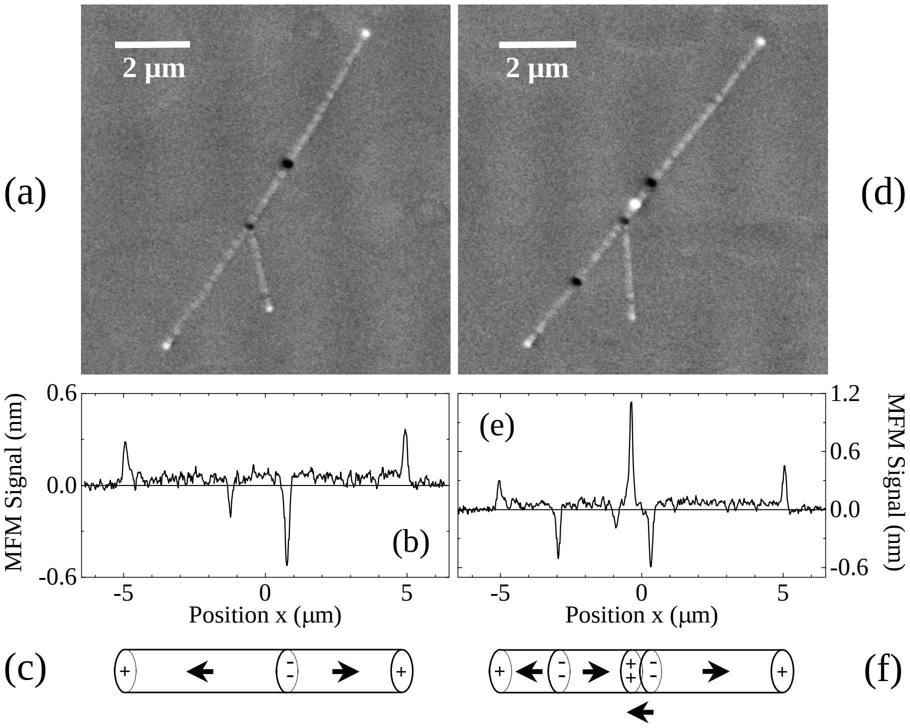

Fig. 12. (a, d) MFM images, (b, e) densitometer traces along the wire axis and (c, f) schematic magnetization distributions for a 10 μm long, 35 nm thick Co nanowire after applying a transverse field of 1.3 T (transverse remanent state). Two sets of data or shown (a–c, d–f) which correspond to two subsequent experiments. Note the presence of a 2 μm long wire fragment the top end of which is sitting on the wire of interest. This fragment is responsible for the weak monopolar dark contrast visible at $x \simeq -1\mu$m (b, e).

nanowire. Again a non-negligible and almost homogeneous contrast is present along both the wire and wire fragment, which can be surely attributed to residual topographical interactions. Contrary to the previous case, the end-contrasts of the unbroken nanowire, which are associated with surface pole distributions on the extreme faces, have now the same polarity; both are indeed bright. This reveals that the axial components of the magnetization in the end regions have opposite orientations. Moreover, a supplementary dark contrast, almost twice as intense as the bright end-contrasts, is detected nearly half way along the wire (Fig. 12b). This corresponds to the strong accumulation of magnetic charges at the boundary between two longitudinally magnetized domains of opposite magnetization directions. In bulk materials and continuous films with in-plane uniaxial anisotropy, 180° domain walls are usually parallel to the magnetization in the domains that they delineate. This arises essentially to avoid net magnetic charges on the walls [22], by virtue of the pole avoidance principle. In contrast, the lateral confinement of the magnetization in small diameter nanowires with parallel-to-wire anisotropy forces the domains to meet head-on and the separating walls to orient perpendicular to the wire axis, hence to the domain magnetization. This results in heavily charged walls having both volume and surface pole distributions, exhibiting therefore strong MFM contrasts, as shown in Figure 12a, b.

Then, the magnetic structure that emerges from the MFM image of Figure 12a is that of a nanowire containing two domains with comparable lengths and opposite axial orientations, as depicted in Figure 12c. The formation of this multi-domain structure can be readily explained as follows. In the transverse saturated state, the magnetization is aligned along the normal to the wire axis, everywhere in the sample. As the strength of the applied field is subsequently reduced, the magnetization that is subjected to a strong torque originating in the parallel-to-wire magnetic anisotropy rotates progressively towards the axial direction. Two regions of the wire which are sufficiently far or decoupled from each other to behave independently may then have their magnetization vectors rotate in opposite directions. In zero field, these two regions eventually give rise to oppositely magnetized domains separated by a 180° wall oriented perpendicular to the wire. Interestingly, the size and the number of domains in which the small diameter wires split when being taken to the transverse remanent state may vary from one experiment to the next. For instance, three, four, five or even nine longitudinally magnetized domains of alternating magnetization directions have been observed in the wire of Figure 12a. A situation with four domains is shown in Figure 12d–f. Notice that the strongly reduced total magnetic moments associated with the multi-domain structures of Figure 12c, f are consistent with the very low transverse remanent magnetization measured on large arrays of similar wires located in their polycarbonate templates (Fig. 2a).

For completeness, we shall mention that, as expected, multi-domain structures similar to those of the transverse remanent state were observed in the transverse demagnetized state obtained by applying an alternating field of slowly decreasing amplitude along the normal to the wire axis. More intriguing are the results obtained on wires in the longitudinal "demagnetized" state. Although a nearly zero remanent magnetic moment was measured on assemblies of several millions of them after the demagnetization procedure, these appeared as single-domain in MFM experiments. There are however additional indications that longitudinally demagnetized assemblies of wires are indeed made of two equally large populations of single-domain cylinders with opposite magnetization (to be presented in a forthcoming paper). Furthermore, the impossibility to observe multi-domain structures in cylinders with large length to diameter aspect ratio after applying an axial field has already been shown by O'Barr *et al.* in the case of Ni cylinders [23].

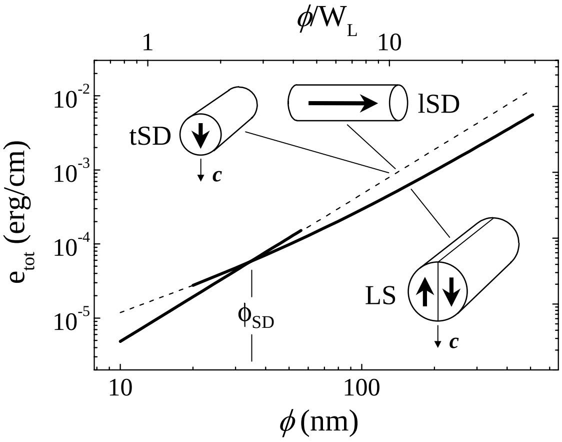

Fig. 13. The magnetic energy per unit of cylinder length of a long cylinder carrying a transverse uniaxial anisotropy $K_u = -6 \times 10^6$ erg/cm^3 as a function of its diameter, for a number of different domain patterns: transverse single-domain (tSD) pattern, longitudinal single-domain (lSD) pattern, and two-stripe (LS) pattern. Above ϕ_{SD} the LS pattern is more favourable than the tSD and lSD patterns which are almost degenerated in energy.

5.2.2 Nanowires with large diameters

A strong similarity exists between Co nanowires with diameters larger than $\phi_{crit} \simeq 50$ nm and single crystal *hcp* (0001) Co films. In both cases, crystal anisotropy (K_u) favours an orientation of the magnetization perpendicular to the direction favoured by shape anisotropy (K_d). In *hcp* (0001) Co thin films with thickness larger than 50 nm, the out-of-plane crystal anisotropy may in circumstances to be described later lead to the formation of perpendicularly magnetized stripe-shaped domains oriented alternately up and down [24]. However, as the anisotropy ratio $Q = |K_u/K_d|$ is less than unity ($Q \simeq 0.4$), the domain structure obeys the Landau model and contains also flux closure domains at the film surface with magnetization parallel to the film plane [25]. Although such a magnetic pattern is associated with sizeable exchange and anisotropy energies due to the numerous domain walls it contains, it has an average energy density smaller than the (anisotropy) energy density K_u of the uniformly in-plane magnetized state, and much smaller than the (demagnetizing) energy density $K_d = 2\pi M_s^2$ of the uniformly magnetized perpendicular state [22].

Cobalt nanowires with diameters significantly larger than ϕ_{crit}, namely with $\phi \geq 100$ nm, are characterised by a strong perpendicular-to-axis uniaxial crystal anisotropy that almost counterbalances shape anisotropy ($K_u = K_1 \sim -6 \times 10^6$ erg/cm^3, $K_d = \pi M_s^2 = 6.2 \times 10^6$ erg/cm^3), hence a Q factor close to unity. Although the wire geometry differs considerably from that of a continuous film, this rather high Q value seems a priori favourable to the formation of parallel-to-wire stripe-like domains with the magnetization oriented transversally along the crystal easy axis, provided of course that the wire diameter be sufficiently large for accommodating such multi-domain magnetic structure. Simple energetic arguments can be developed to convince ourselves that such magnetic structure may be stable. Let us consider the simple case of a magnetic cylinder with diameter ϕ and length much larger than ϕ, carrying a uniaxial perpendicular-to-axis crystal anisotropy K_u. The cylinder cross-section is hypothetically subdivided into two transversally magnetized domains of opposite magnetization ($\mathbf{M}$ parallel to the crystal easy axis) and equal volumes extending along the whole cylinder length, *i.e.* two longitudinal stripes (LS). These are separated by a 180° Bloch wall with energy $\sigma_w = 4\sqrt{A|K_u|}$ per unit surface (A being the exchange stiffness constant), whose thickness is assumed to be negligible compared to ϕ. For simplicity, we shall consider a fully flux-opened pattern associated with a zero crystal energy, as sketched in Figure 13 (LS pattern).

Per unit of cylinder length, the total energy of this domain structure is

$$e_{tot} = \sigma_w \phi + \eta \pi K_d \phi^2/4 \tag{4}$$

where η is the factor by which the average demagnetizing energy density of the longitudinal-stripe domain state ($\eta\pi M_s^2$) is lowered as compared to that of the uniformly perpendicular-to-wire magnetized state ($K_d = \pi M_s^2$). It is beyond the scope of this paper to present a comprehensive calculation of the factor η. Therefore, we shall just mention the value of $\eta = 0.40$ computed by Ebels and Buda [26]. Using this together with the exchange stiffness of bulk cobalt $A = 1.03 \times 10^{-6}$ erg/cm [27] and the $K_u = K_1$ of -6×10^6 erg/cm^3 determined experimentally ($\sigma_w = 10$ erg/cm^2), we find indeed that for cylinder diameters larger than $\phi_{SD} \simeq 34$ nm the LS state has a lower energy than both the transverse single-domain (tSD) state ($e_{tot} = \pi K_d \phi^2/4$) and the longitudinal single-domain (lSD) state ($e_{tot} = \pi K_u \phi^2/4$), which are almost degenerated in energy (Fig. 13). One should however

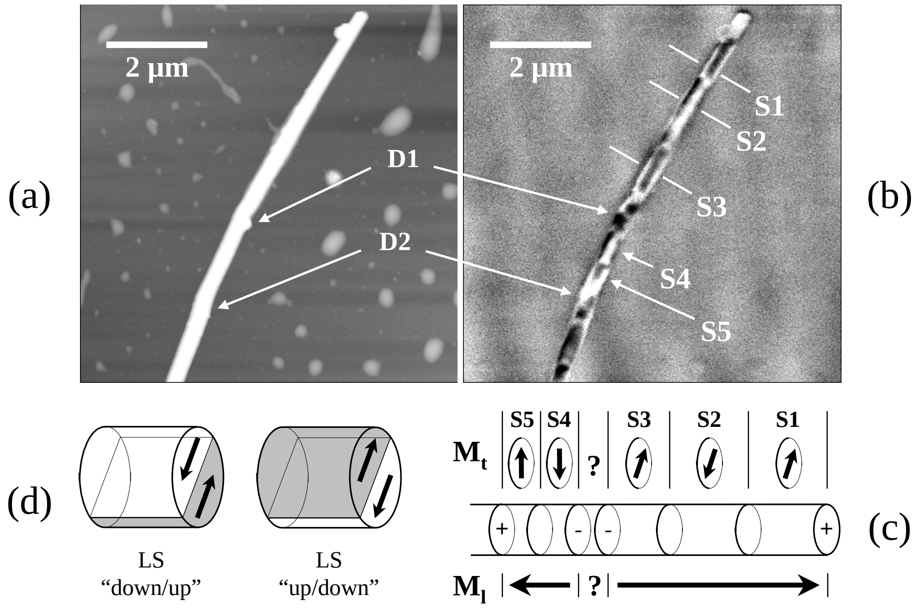

Fig. 14. AFM (a) and MFM (b) images of a 10 μm long, 150 nm thick Co nanowire after applying a transverse field of 1.3 T (transverse remanent state). The bottom part of the wire is not shown as it could not be satisfactorily imaged because of the presence of a large metal residue from the cathode Cu film. (c) Possible orientation of the transverse ($\mathbf{M}_\mathrm{t}$) and longitudinal ($\mathbf{M}_\mathrm{l}$) magnetization components (see text for details). (d) Schematic representation of cylinder portions in the so-called "up/down" and "down/up" longitudinal-stripe (LS) magnetic configurations.

emphasise that the validity of our model is somewhat questionable since the assumption we made of a thin domain wall compared to the wire diameter is not valid throughout the full diameter range considered in Figure 13; it is especially not valid below and around ϕ_SD. Indeed, the width of 180° walls in uniaxial crystals is known to amount approximately to $W_L = \pi\sqrt{A/|K_\mathrm{u}|}$, that is $W_L \simeq$ 13 nm in our case, which is only 3 times smaller than the transition diameter $\phi_\mathrm{SD} \simeq 34$ nm. A true micromagnetic modelling would then be required to determine a correct single-domain limit ϕ_SD. Nevertheless, our result concerning the relative stability of the single-domain (tSD and lSD) states and LS state holds true for larger diameters, typically those such that $\phi/W_L > 10$, which includes the diameters of interest ($\phi \geq 100$ nm). Although not a case described by the previous model, nanowires might also subdivide into more than two stripes, for large enough diameters. Moreover, since the Q factor has an intermediate value (neither small nor very large), the magnetic ground state in large diameter wires might resemble the Landau model for thin films and also exhibit flux closure domains, with magnetization perpendicular to the crystal easy axis. None of these possibilities will however be further considered in the following.

In *hcp* (0001) Co films with thickness in the range of 50 to 500 nm, a manifold of (meta-) stable patterns with perpendicularly magnetized domains may be observed in zero field depending on the magnetic history of the films [24,28]: (i) intricate elongated bubbles are obtained after saturation in a perpendicular-to-plane field, (ii) a maze pattern of labyrinthine stripes is formed after demagnetization with a perpendicular alternating field, (iii) more importantly, a regular pattern of parallel stripe domains is generated by demagnetizing the film with an alternating magnetic field applied in the film plane, the direction of this field determining that of the stripes, and finally (iv) a mixed pattern of bubbles and bands is obtained after saturation in a field parallel to the film plane. Among these patterns, it is generally admitted that the stripe pattern whose formation was explained by Muller [29] is energetically the more favourable in zero field and hence constitutes the magnetic ground state [30].

The MFM images taken on Co nanowires with 100 nm $\leq \phi \leq$ 200 nm (that is the range of large diameters to which we restricted our MFM investigations) have not revealed such a richness in the possible domain structures, probably due to the one-dimensional-like geometry of the samples. The most frequently observed kind of image is shown in Figure 14b. This particular image was obtained on a 150 nm thick, 10 μm long wire after saturation by means of a transverse field (transverse remanent state). However similar contrasts were also recorded after demagnetization with a transverse field (transverse demagnetized states). One may first notice that, contrary to the case of the small diameter wires described previously, strong and complex contrasts are now visible all along the wire length, which are magnetic in origin as they proved to reverse upon reversal of the tip magnetization. These are the signature of a large transverse component of the magnetization. Besides, the wire image of Figure 14b appears as being made of several segments with block-wise varying MFM contrasts. Inside each segment the contrasts are qualitatively invariant upon translation along the wire axis. When passing from one segment to the next the contrasts globally invert as can be seen from the alternation of dark and bright contrasts along the sides and the top

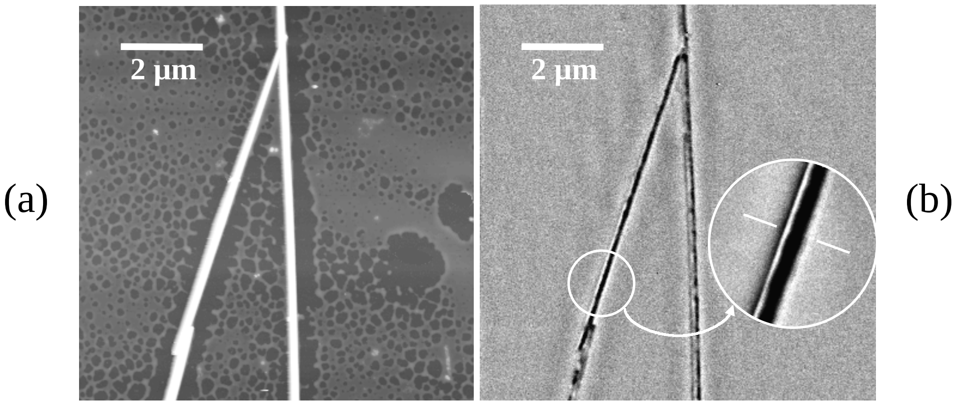

Fig. 15. AFM (a) and MFM (b) images of a 11.5 μm long, 120 nm thick wire fragment with well defined magnetic contrasts interacting with other fragments of ill-defined contrasts close to its upper and lower ends. These images were recorded after demagnetization by means of an alternating axial field of slowly decreasing amplitude (longitudinal demagnetized state). Inset in (b): Zoom of the MFM contrasts in the region delineated by a circle.

generatrix of the cylinder. While two of the boundaries between segments are clearly related to topographical features, namely cracks or grain boundaries detectable in the AFM image of Figure 14a (defects labelled D1 and D2), most of them have no visible topographical counterparts. Furthermore, the length of the segments ranges typically from 0.5 to 1.5 μm with a maximum in the length distribution at about 1 μm, as deduced from MFM observations of several wires. This is significantly smaller than the length of the Co grains visualised by TEM, which is several micrometers [17]. Therefore, it is believed that several segments may emanate from a given single crystal region. In the following, the word "segment" will be used indifferently to indicate a region of longitudinally invariant MFM contrasts and the corresponding wire portion.

Although not always visible, monopolar-like contrasts are sometimes detected which span the ends of the large diameter wires (see top end of the wire of Fig. 14b). These reveal that the magnetization may have a non-zero axial component. One might thus be tempted to associate segments with regions of alternating axial magnetization component. However, if this were the case, monopolar contrasts even stronger than the end contrasts should be *systematically* recorded at the segments boundaries, as is observed for multi-domain wires of small diameters (Fig. 12). This is not verified experimentally.

The MFM contrasts recorded after longitudinal saturation or demagnetization (field applied along the wire axis) qualitatively resemble those obtained after transverse saturation or demagnetization. Indeed these exhibit the same kind of "bamboo" structures seen in Figure 14b. A major difference however exists in the length of the segments observed. In the longitudinal demagnetized and remanent states, segments are generally much longer (several micrometers long). One single segment may even extend over the full cylinder length. This can be seen in Figure 15 which shows the AFM (Fig. 15a) and MFM (Fig. 15b) images of a 11.5 μm long, 120 nm thick wire fragment in the longitudinal demagnetized state, interacting at its two ends with other wire fragments of ill-defined MFM contrasts. In view of the lengths involved, the segments are now most probably delineating single crystal regions. In agreement with the structural characterisation by TEM, we may reasonably assume that from one segment to the next the c-axis rotates in a plane perpendicular to the wire axis. Owing to this view, the wire fragment of Figure 15 appears as being essentially single crystal and, more important, the change of MFM contrasts from segment to segment may be ascribed to a modification of the transverse component of the magnetization, a contrast inversion reflecting a reversal of the transverse magnetization component.

In their study of similar electrodeposited cobalt nanowires with diameters of the order of 80–90 nm, Belliard *et al.* reported the same kind of segment structures as shown here [9]. These authors observed strong dipolar end-contrasts *after longitudinal saturation* and thus concluded that the magnetization had to remain mostly axial in the studied wire fragments. They attributed the change of MFM contrasts from segment to segment (or grain to grain) to fluctuations in the magnetization distribution around the wire axis. The magnetic pattern in the wires was finally described as being made of a succession of cylindrical domains with the magnetization at an angle from the wire axis, the axial magnetization component in each of these domains pointing in the same direction (imposed by the saturating field), the transverse component fluctuating from domain to domain due to changes in the orientation of the c-axis (Fig. 5g in Ref. [9]). To support this view and extract the orientation of the off-axis magnetization, MFM contrasts across the wires were fit assuming that segments were corresponding to *homogeneously magnetized wire portions* [9].

A similar fitting procedure based on equations (B.2) and (B.10) was applied here with varying degrees of success to densitometer traces along line scan perpendicular to the cylinders axis. The main adjustable parameters were the effective lift height of the equivalent tip dipole and the angle φ of the transverse magnetization component with respect to the $\hat{\mathbf{z}}$ axis. Moreover, the centre of

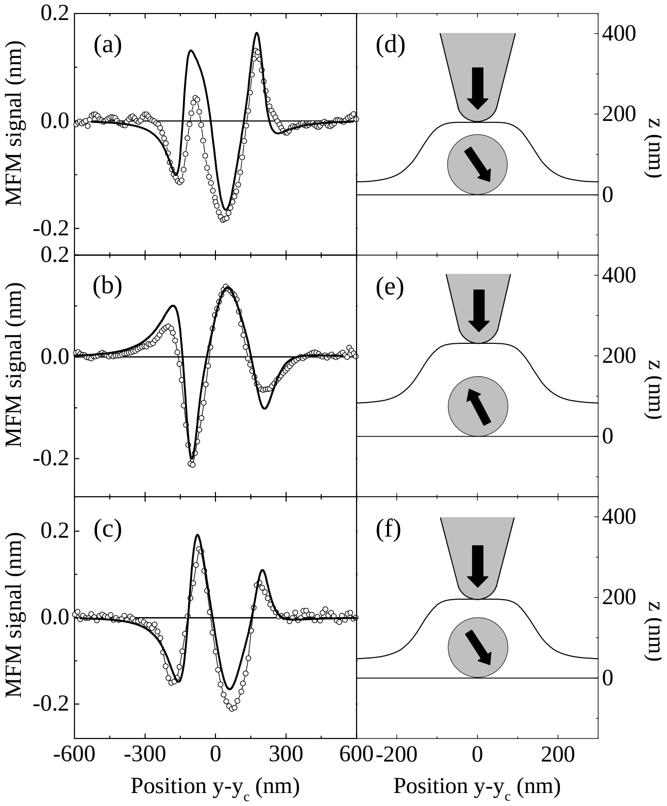

Fig. 16. (a–c) MFM contrasts across segments (a) S1, (b) S2 and (c) S3 in Figure 14(b) (open circle) and fits to the experimental data (thick solid line) assuming segments with homogeneous transverse magnetization component. (d–f) Orientation of the transverse magnetization component in segments (d) S1, (e) S2 and (f) S3 as deduced from the fit. The solid lines indicate the trajectories of the equivalent tip dipole (see text for details).

the cylinder was allowed to be slightly displaced (a few nanometers) with respect to the symmetry plane of the tip trajectory to account for a possible asymmetry in the thickness of the polycarbonate redeposit along the wire sides. Let us first consider the MFM contrasts within the three segments (labelled S1 to S3 from top to bottom) contained in the region extending from a short distance to the top end of the wire of Figure 14b to what was previously identified as a first crystal defect (D1 in Fig. 14b), a region which we suspect is single crystal. Densitometer traces across these segments and fits to the experimental data are shown in Figure 16a–c. Although quantitative accurate fits could not always be obtained, *all* of the main features discernible along the traces are reproduced. As suggested earlier in this paper and emphasised by Belliard and co-workers, it is only when using realistic probe trajectories, hence taking into account the sample topography parameterised with equation 3 ($H \simeq 150$ nm, $2L \simeq 290$ nm, $n = 4$ or 6), that one is able to match the “extrinsic” narrow peak contrasts appearing on the sides of the wire. The orientation of the transverse magnetization component in each of the three wire segments as deduced from the fitting procedure is indicated in Figure 16d–f. It is noteworthy that the two extreme segments S1 and S3 have their off-axis magnetization components almost parallel ($\varphi_1 = 141°, \varphi_3 = 145°$) while the transverse magnetization in the intermediate segment S2 has a nearly opposite orientation ($\varphi_2 = -32°$). This observation provides a strong indication that the orientation of the *c*-axis is the same in all three segments. The region investigated is then very likely single crystal, as suspected. The same conclusion may be drawn from the fit (not reported here) of densitometer traces across the two segments (labelled S4 and S5) located between D1 and D2 (Fig. 14): These two segments also seem to have antiparallel transverse magnetization components ($\varphi_4 = -5°, \varphi_5 = 178°$) and thus probably belong to the same crystal grain. Note that this conclusion could have been reached without fitting the MFM profiles but simply by noticing that the contrasts almost perfectly invert from one segment to the next (Fig. 16a–c). Therefore it does not necessarily rely upon the assumption we made up to now of homogeneously magnetized segments. As a summary, a possible magnetization distribution within the five topmost segments of the wire of Figure 14b is sketched in Figure 14c, which for its part relies on the assumption of *homogeneously magnetized segments*. The orientation of the transverse magnetization component ($\mathbf{M}_t$) was deduced from our fitting procedure. The direction of the longitudinal component ($\mathbf{M}_l$) was inferred from the monopolar-like contrasts visible at the wire top end (bright contrast) and at the location of defects D1 (double dark contrast) and D2 (bright contrast). Note that the existence of a weak longitudinal magnetization component is consistent with a slight misalignment of the crystal easy axis with respect to the wire normal, as that shown in Figure 4c.

The fact that region A (segments 1, 2 and 3) and region B (segments 4 and 5) have opposite longitudinal magnetization components after transverse saturation may be readily explained using the same argument as the one given to account for the domain structures observed in small diameter wires brought to the transverse remanent state (Sect. 5.2.1): A truly transverse field does not favour any of the two longitudinal directions. Hence, when reducing the applied field, the magnetization may rotate indifferently towards any of these two directions. The fact that single crystal regions several micrometers long, such as regions A and B, seem to split into homogeneously magnetized cylindrical domains of average length 1 μm and alternating transverse magnetization component (Fig. 14c) is more puzzling. Indeed, as the field is decreased, the transverse magnetization component is rather expected to rotate as a whole towards that of the two directions colinear to the *c*-axis which is the closest to the field direction (considering the general case where $\mathbf{H}$ is not parallel to $\mathbf{c}$). A gain in demagnetizing energy following the splitting in domains may of course be invoked as an explanation. However, given the length of the segments, this gain is expected to be small, very likely smaller than the increase in magnetic energy due to the introduction of domain walls between segments. Another possible explanation is that the transverse saturating field, applied prior

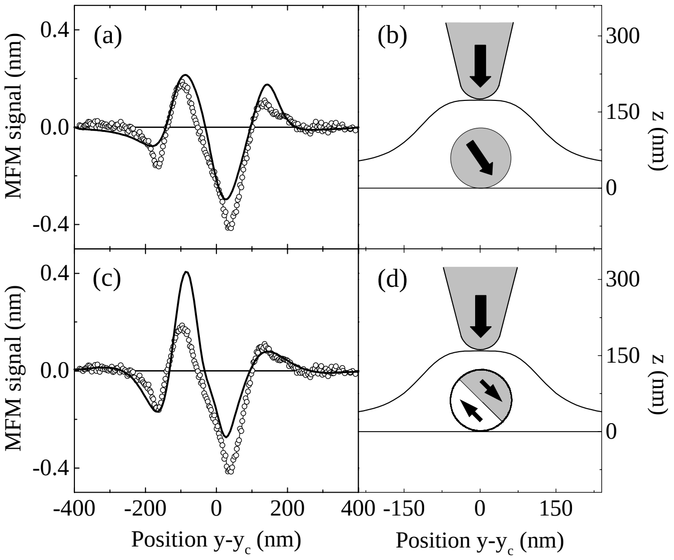

Fig. 17. (a, c) MFM contrasts across the wire fragment of Figure 15 (open circle). The thick solid lines are: (a) a fit to the experimental data assuming a homogeneous transverse magnetization component as sketched in (b), (c) a simulation assuming the magnetization distribution sketched in (d).

to the membrane dissolution at an unknown angle, was by chance oriented perpendicular to the crystal easy axis so that none of the two transverse directions colinear to **c** was favoured as the field was turned off and domains with the two transverse orientations could form. However, how could the field have been applied perpendicular to the c-axes of grains A and B while these axes are seemingly oriented 30° apart from each other (compare φ_1 and φ_5)?

Let us now concentrate on the longitudinally invariant MFM contrasts recorded on the single-crystal wire fragment of Figure 15b. These contrasts qualitatively resemble those of segments 1 and 3 in Figure 14b. In the present case, the absence of discernible monopolar end contrasts, especially at the bottom end of the fragment a small part of which only is hidden by a neighbouring fragment, indicates that the magnetization is mostly oriented perpendicular to the cylinder axis. A densitometer trace across the discussed contrasts is shown in Figure 17a. Here again a fit based on equations (B.2) and (B.10) and including a realistic tip trajectory ($H = 130$ nm, $2L \simeq 260$ nm, $n = 4$) allows to reproduce well, though not perfectly, the main experimental features. The orientation of the transverse magnetization component as deduced from the fitting procedure is indicated in Figure 17b ($\varphi = 147°$). MFM contrasts thus seem to support the idea of a single domain mostly transversally magnetized wire fragment. However, energetic arguments developed earlier have shown that such a magnetic pattern (tSD pattern in Fig. 13) is significantly less stable than that consisting of two parallel-to-wire stripes of opposite transverse magnetization (LS pattern in Fig. 13). Furthermore, the magnetic image of Figure 15b was obtained after demagnetization by means of an axial field. If one notes that in *hcp* (0001) Co thin films an analogous demagnetization procedure (with $\mathbf{H} \perp \mathbf{c}$) leads to the formation of perpendicularly magnetized stripe domains extending along the direction of the demagnetizing field, one may be tempted, by analogy, to associate the observed longitudinally invariant contrasts to the LS magnetic pattern of Figure 13.

In order to put this possibility to the test and compute the MFM response expected for the LS magnetization configuration, we developed also a *purely numerical approach* (as opposed to the analytical approach used so far, see Appendix B). It is similar to the one used by Wadas to calculate the magnetic forces experienced by a magnetic tip during MFM experiments [31]. In this approach, the magnetized cylinder (magnetization M) is subdivided into cubic finite elements whose edge d is much smaller than the cylinder diameter ϕ so as to ensure a fairly smooth surface of the discretized wire. Each of the cubic elements is located at a nod of a simple cubic three-dimensional mesh with position vector $\mathbf{r}_{ijk}$ and is assumed to contain a point magnetic moment $\boldsymbol{\mu}_{ijk}$. Its contribution to the total stray field $\mathbf{H}$ emanating from the cylinder is given by the classical expression for the field generated by a point dipole

$$\mathbf{H} = \frac{3\left[\boldsymbol{\mu}_{ijk}\cdot(\mathbf{r}-\mathbf{r}_{ijk})\right](\mathbf{r}-\mathbf{r}_{ijk})}{\left|\mathbf{r}-\mathbf{r}_{ijk}\right|^{5}} - \frac{\boldsymbol{\mu}_{ijk}}{\left|\mathbf{r}-\mathbf{r}_{ijk}\right|^{3}} \tag{5}$$

with $\mathbf{r} = x\hat{\mathbf{x}} + y\hat{\mathbf{y}} + z\hat{\mathbf{z}}$, $\mathbf{r}_{ijk} = d\,(i\hat{\mathbf{x}} + j\hat{\mathbf{y}} + k\hat{\mathbf{z}})$ and $\boldsymbol{\mu}_{ijk} = Md^3\,(\alpha_{ijk}\hat{\mathbf{x}} + \beta_{ijk}\hat{\mathbf{y}} + \gamma_{ijk}\hat{\mathbf{z}})$, where i, j and k are integers and α_{ijk}, β_{ijk} and γ_{ijk} are the direction cosines of the magnetic moment $\boldsymbol{\mu}_{ijk}$ with respect to the x, y and z axes. The magnetic force gradient experienced by the probing tip is obtained by adding the contributions from all finite elements which contain a magnetic moment that interacts effectively with the equivalent magnetic moment of the tip $\mathbf{m}$. Thus, under the assumptions listed in Appendix B, the magnetic force derivative (Eq. (B.2)) takes the form

$$F'_{\mathrm{mag}} = m\sum_{i,j,k}\frac{\partial^2\left(\mathbf{H}_{ijk}\cdot\hat{\mathbf{z}}\right)}{\partial z^2} \tag{6}$$

from which it comes

$$\begin{aligned} F'_{\mathrm{mag}} = mMd^3\sum_{i,j,k} & \frac{9\gamma_{ijk}}{\left[(x-id)^2+(y-jd)^2+(z-kd)^2\right]^{\frac{5}{2}}} \\ & - \frac{45\left[\alpha_{ijk}(x-id)+\beta_{ijk}(y-jd)+2\gamma_{ijk}(z-kd)\right](z-kd)}{\left[(x-id)^2+(y-jd)^2+(z-kd)^2\right]^{\frac{7}{2}}} \\ & + \frac{105\left[\alpha_{ijk}(x-id)+\beta_{ijk}(y-jd)+\gamma_{ijk}(z-kd)\right](z-kd)^3}{\left[(x-id)^2+(y-jd)^2+(z-kd)^2\right]^{\frac{9}{2}}}. \end{aligned} \tag{7}$$

In an attempt to simulate the MFM contrasts of Figure 15b, calculations with $d = \phi/51$ ($-25 \leq j, k \leq 25$, $j^2 + k^2 \leq 25^2$) were performed in which the integration along the wire axis ($\hat{\mathbf{x}}$ axis) was restricted to the finite elements such that $-100 \leq i \leq 100$. Taking into account elements with $|i| > 100$ proved to have negligible influence

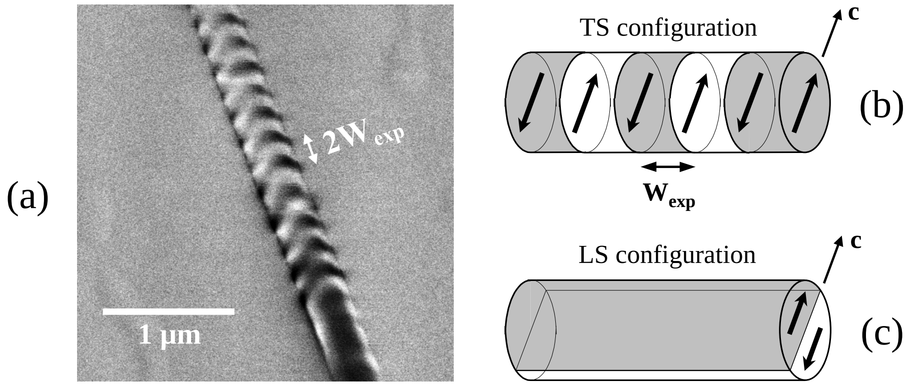

Fig. 18. (a) High resolution MFM image of a portion of a Co nanowire, 150 nm in diameter, in a virgin magnetic state. The strong difference in the MFM contrasts observed on the top and bottom parts of this wire reflects a deep change in the magnetization distribution. (b, c) Possible domain structures in (b) the top part and (c) the bottom part of the wire imaged in (a).

on the computed MFM signal. Figure 17c compares the experimental data with a rather successful simulation corresponding to the situation depicted in Figure 17d (magnetization in the stripe domains oriented at $-45°$ and $135°$ from the $\hat{\mathbf{z}}$ axis). Although the amplitudes of the two innermost peak contrasts are not matched, the large difference in the width of these peaks of comparable height and, more important, the particular shape of the MFM profile around $y - y_{\rm c} = 0$ are remarkably well reproduced (with regard to the simplicity of the model), as are also the shape and the amplitude of the side contrasts. Moreover, other simulations not shown here were made in which the amplitudes of the central peak contrasts were better matched but their shapes not so accurately fit. Thus, both of the simple models used to simulate the MFM contrasts of Figure 15b allow to reproduce the experimental data with a certain accuracy. This highlights the difficulty to distinguish the tSD and LS magnetic patterns from MFM experiments.

Before concluding about the segment images, we shall mention that peculiar MFM contrasts were sometimes observed on Co nanowires with large diameters *in a virgin magnetic state*, which could not be re-observed after a magnetic field of significant amplitude was applied. The image of Figure 18a shows such contrasts, obtained on a portion of a 150 nm thick wire. While the bottom part of it presents the same kind of longitudinally invariant contrast as discussed before (segment), the top part reveals a rapid alternation of pairs of diametrically opposed dark and bright contrasts along the wire. These contrasts are qualitatively periodic with a period of $2W_{\rm exp} \simeq 200$ nm. It is believed that they correspond to a magnetic configuration (labeled TS) made of short cylindrical domains with antiparallel transverse magnetization ($\mathbf{M} \parallel \mathbf{c}$) (Fig. 18b). To keep on drawing a parallel with magnetic domain structures in *hcp* (0001) Co films, these would be equivalent to stripe domains extending transversally. To justify the existence of such a magnetic configuration it is noted that the longitudinal extension of the domains $W_{\rm exp} \simeq 100$ nm, *i.e.* the width of the stripes, is sufficiently small here so that a very strong reduction of demagnetizing energy is expected to be realised in comparison with the transverse single-domain (tSD) state.

Moreover, three dimensional finite element calculations [32], considering a magnetic bar carrying a transverse crystal anisotropy $K_{\rm u} = -6 \times 10^6$ erg/cm^3, are currently in progress, which have already shown that, for bar dimensions close to those of our cylindrical wires, the TS pattern is indeed the state of lowest magnetic energy as compared to all the other magnetic configurations (tSD, lSD, LS) considered in this work [26]. Assuming a domain wall energy of $\sigma_{\rm w} = 16$ erg/cm^2, a domain width of $W_{\rm cal} = (100 \pm 2)$ nm has been found to minimise the total energy of the TS configuration, in excellent agreement with the present observations. This result does not support the idea that the segment images of Figure 14b may correspond to cylindrical domains of alternating homogeneous transverse magnetization since these segments have a length of the order of 1 μm, that is much larger than $W_{\rm cal} \simeq W_{\rm exp}$. Indeed, why would the width of the transversally magnetized domains vary so strongly from wire to wire, or from one region to another in a given wire (see Fig. 18a)? Interestingly, the finite element calculations have also shown that the TS and LS configurations have almost equal magnetic energies, though, as mentioned before, the TS state appears as the state of lowest energy. This may explain why these two configurations are seemingly coexisting in the wire of Figure 18a. However, it is not yet understood why the TS configuration was only observed in nanowires in a virgin magnetic state.

To summarise, segment images (Fig. 14b) might well correspond to cylindrical domains of homogeneous transverse magnetization component, as suggested by Belliard *et al.* [9] from their study of similar Co nanowires with $\phi = 80 - 90$ nm. However, when applied to nanowires with $100 \text{ nm} \leq \phi \leq 200$ nm, this interpretation raises questions to which answers have not been found yet. Segments might also correspond to cylinder portions split into two stripe-like domains of opposite transverse magnetization component, which seems energetically more favourable, at least for $\phi > 100$ nm, and is therefore the interpretation favoured by the authors. This second interpretation offers the advantage of giving a satisfactory answer to the question as to why several segments of inverse MFM contrasts may coexist in a single crystal wire region after transverse saturation. In this case indeed, an inversion of contrasts from one segment to the next (Fig. 16a–c), would indicate a transition from a wire portion with stripe domains oriented "up/down" to a wire portion with stripe domains oriented "down/up" (Fig. 14d). These two configurations are intrinsically equivalent whatever the orientation of the transverse field applied previously. Therefore they are equally likely to occur in zero field and single crystal regions may reasonably split into segments with alternating LS magnetic configuration. We wish to emphasize that the conclusion of the present study and the conclusion of the work of reference [9] are not necessarily contradictory as the range of wire diameters investigated in the two cases are different. It might even be the case that both of them are correct and that the ground state magnetic configuration changes from tSD-like to LS-like at $\phi \simeq 100$ nm. Whatever interpretation is correct, the MFM observations confirm that, as the external field is reduced, domains form in large diameter Co nanowires, in which the magnetization has a strong transverse component, a result already suggested by the analysis of low field magnetic torque curves.

6 Conclusion

Cobalt cylindrical nanowires with length of 10 or 20 μm and diameters ϕ in the range of 30 to 450 nm were grown by electrodeposition in the pores of track-etched polymer membranes. These are made of large crystal grains of *hcp* structure extending transversally across the full wire diameter and longitudinally over several micrometers. As the wire diameter is reduced below $\phi_{\text{crit}} \simeq 50$ nm the preferential orientation of the crystal easy axis of magnetization (c-axis) changes from perpendicular to parallel to the wire axis. This was shown to determine the zero field magnetic domain structure forming in the nanowires.

For small diameters ($\phi < \phi_{\text{crit}}$), both shape anisotropy and magnetocrystalline anisotropy favour an alignment of the magnetization along the wire axis. As a consequence, the magnetization is mostly oriented longitudinally and a single domain structure can be realised after applying a saturating magnetic field parallel to the wire. After the application of a transverse saturating field, the magnetic configuration consists of a succession of longitudinally magnetized antiparallel domains, whose number may vary between two and ten (typically, in 10 μm long wires). Due to the severe lateral confinement of the magnetization, these domains are forced to meet head-on. Hence, the separating domain walls carry a large amount of magnetic charges. It is noteworthy that such a domain geometry is highly favourable to the observation of a domain wall magnetoresistance (DW-MR) effect. Indeed, provided that the external field be applied along the wire axis, no parasitic MR effect such as anisotropic magnetoresistance is expected to show up here [33].

In nanowires with large diameters ($\phi > \phi_{\text{crit}}$), a longitudinal single domain state cannot be achieved in zero field, although the very elongated shape of the objects favours such a magnetic configuration. Instead, complex multidomain patterns always form in zero field, in which the domain magnetization has a strong transverse component. This results from a competition between the shape anisotropy and the magnetocrystalline anisotropy which tends to align the magnetization normal (or almost normal) to the wire axis. On the basis of energetic arguments and considering the strong similarity that exists between these cobalt nanowires and thin cobalt films with strong out-of-plane crystal anisotropy it was further suggested that, for $100 \text{ nm} \leq \phi \leq 200$ nm, the zero field domain structures generally consist of a succession of cylinder portions containing two parallel-to-wire stripe-like domains with opposite transverse magnetization component.

Finally, the origin of the change of crystallographic texture of Co as the wire diameter is varied is left as an opened question. It may be related to a local increase of pH in the pores of smaller diameter, were the Boric acid could not fully play its buffering action. Indeed, it is well known that variations of pH can strongly affect the crystallographic properties of plated Co films [15]. However, no firm conclusion can be drawn yet in the case of our Co nanowires.

The authors wish to thank R. Legras and E. Ferain for providing the polycarbonate membrane samples used in this work, and U. Ebels, L. Buda and L. Prejbeanu for fruitful discussions. V. Da Costa and C. Uhlac-Bouillet are gratefully acknowledged for their experimental support. L.P. is a Research Associate of the National Fund for Scientific Research (Belgium). This work was partly supported by the EC-Growth Project GRD1-1999-10428, as well as by the Belgian Interuniversity Attraction Pole Program (PAI-IUAP P4/10).

Appendix A: Principle of the magnetic force microscopy in the tapping/lift$^{\text{TM}}$ mode

In the tapping/lift^{TM} interlace technique developed by Digital Instruments, the microscope is operated in a non-contact, *ac* detection mode. Then, such a detection technique yields a signal related to the derivative of the force acting the probing tip $F' = \hat{\mathbf{n}} \cdot \nabla(\hat{\mathbf{n}} \cdot \mathbf{F})$, where $\hat{\mathbf{n}}$ is a unit vector perpendicular to the cantilever that supports the tip [21]. This particular technique allows disentangling the topographical and magnetic data and to collect both kinds of information during the same image acquisition, making easy the correlation of the magnetic data with topographical features. Magnetic interactions are separated from topographical interactions using a two-pass scanning method [34]. During the first pass, the oscillating tip, which flies very near to the sample surface, is mainly subjected to short range Van der Waals forces hence images the surface topography. During the second pass, the tip-sample distance is increased by some preprogrammed amount (typically 15 to 50 nm for the reported experiments), chosen so that the lifted tip be then predominantly subjected to long range magnetic forces due to dipolar interactions between the tip magnetization and the stray field emanating from the specimen. The tip is driven along a trajectory that mimics precisely the sample topography measured during the first pass. The recorded signal then consists of the variation of the magnetic force gradient at constant height above the specimen surface.

Appendix B: Modelling of the MFM response

One simple but very instructive approximation that we used for modelling the MFM response of the nanowires is to assume that the probing tip consists of a point dipole with effective magnetic moment $\mathbf{m}$. In this case, the magnetic force acting on the tip follows the equation

$$\mathbf{F}_{\mathrm{mag}} = \nabla(\mathbf{m} \cdot \mathbf{h}) \tag{B.1}$$

where $\mathbf{h}$ is the stray field from the sample under investigation. If, as is usual and was always the case for the reported MFM experiments, the cantilever is vibrated along the $\hat{\mathbf{z}}$ axis perpendicular to the $x - y$ plane in which the flat substrate supporting the sample lies ($\hat{\mathbf{n}} = \hat{\mathbf{z}}$) and if the effective magnetic moment of the tip is oriented along the $\pm\hat{\mathbf{z}}$ direction ($m_x = m_y = 0, m_z = \pm m$), the magnetic force derivative to which the MFM response is proportional reads

$$F'_{\mathrm{mag}} = \pm m \frac{\partial^2 h_z}{\partial z^2} \cdot \tag{B.2}$$

Thus, the MFM response is simply proportional to the second derivative with respect to the z coordinate of the vertical component of the stray field produced by the sample at the tip location [21]. It should be emphasised that this approach is only valid under the additional assumption that the stray field from the sample is not sufficient to alter the magnetization in the tip and that, conversely, the stray field from the tip has no significant effect on the magnetization distribution within the sample. We believe that this is the case for the magnetically hard tips used and the highly anisotropic and coercive Co nanowires studied.

Analytical expressions for the z component of the stray field generated by a *uniformly magnetized straight cylinder* of radius R and the revolution axis of which is parallel to the $\hat{\mathbf{x}}$ direction can be obtained in two particular cases which are relevant in the present study.

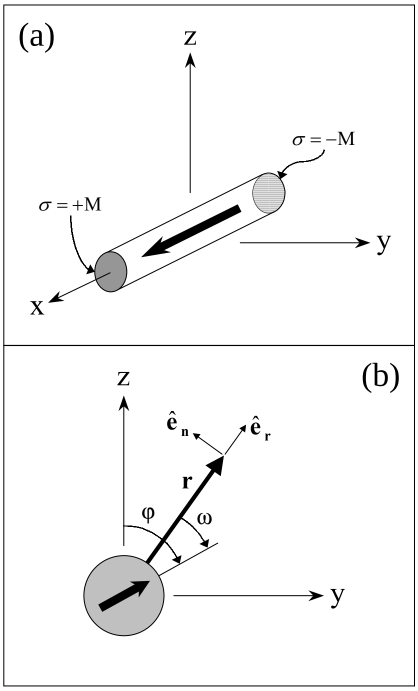

Fig. 19. (a) Magnetic charges with surface densities $\sigma = +M$ and $\sigma = -M$ on the end faces of a longitudinally magnetized cylinder ($\mathbf{M} \parallel \hat{\mathbf{x}}$). (b) The angles for the calculation of the stray field generated by an infinite transversally magnetized cylinder ($\mathbf{M}$ in the $y - z$ plane).

(i) We first consider the case of a *longitudinally magnetized cylinder* (magnetization $\mathbf{M}$ parallel to $\hat{\mathbf{x}}$) of finite length L. For such a cylinder, the stray field can be regarded as the superposition of the magnetic fields created by two discs having $\sigma = +M$ and $\sigma = -M$ as surface pole densities, which correspond to the two circular end faces of the cylinder (Fig. 19a). According to literature [35], the z or radial component of the field from a disc with diameter R, perpendicular to the $\hat{\mathbf{x}}$ direction, centred at $x = x_0$ and having a uniform surface pole density of σ is

$$h_z = \frac{\sigma\sqrt{R}}{\pi k \sqrt{z}} \left[\left(1 - \frac{k^2}{2}\right) K(k) - E(k) \right]$$
$$\text{with} \quad k^2 = \frac{4Rz}{(R+z)^2 + (x - x_0)^2} \tag{B.3}$$

where $K(k)$ and $E(k)$ are the complete elliptic integrals of first and second kind respectively, which may be differentiated to give

$$\frac{\mathrm{d}K}{\mathrm{d}k} = \frac{E}{k\,(1-k^2)} - \frac{K}{k}$$
$$\frac{\mathrm{d}E}{\mathrm{d}k} = \frac{E}{k} - \frac{K}{k} \cdot \tag{B.4}$$

Using equations (B.4), the second derivative of h_z with respect to z can be calculated and expressed in terms of elliptic integrals as

$$\frac{\partial^2 h_z}{\partial z^2} = \left(\frac{\sigma}{4\pi}\right) \left[A_K K(k) + A_E E(k) \right] \tag{B.5}$$

with

$$A_K = \frac{5\left[R^2+(x-x_0)^2\right]}{z^3\left[(R+z)^2+(x-x_0)^2\right]^{\frac{1}{2}}} - \frac{\left\{\left[R^2+(x-x_0)^2\right]^2-z^2\left[R^2-(x-x_0)^2\right]\right\}\left[R^2-z^2+(x-x_0)^2\right]}{z^3\left[(R+z)^2+(x-x_0)^2\right]^{\frac{3}{2}}\left[(R-z)^2+(x-x_0)^2\right]} \tag{B.6}$$

and

$$A_E = \frac{z^2\left[R^2+(x-x_0)^2\right]-5\left[R^2+(x-x_0)^2\right]^2}{z^3\left[(R+z)^2+(x-x_0)^2\right]^{\frac{1}{2}}\left[(R-z)^2+(x-x_0)^2\right]} + \frac{\left[R^2+(x-x_0)^2\right]^2-z^2\left[R^2-(x-x_0)^2\right]}{z^3\left[(R+z)^2+(x-x_0)^2\right]^{\frac{3}{2}}\left[(R-z)^2+(x-x_0)^2\right]^2} \times\left[\left(R^2-z^2\right)\left(R^2+7z^2\right)+2\left(R^2-3z^2\right)(x-x_0)^2 +(x-x_0)^4\right]. \tag{B.7}$$

Applying these to two discs with $\sigma = \pm M$ located at $x_0 = \pm L/2$, the stray field from an axially magnetized cylinder and its second derivative can be readily calculated.

(ii) The second case that we consider is that of an *infinitely long transversally magnetized cylinder* [36] (magnetization $\mathbf{M}$ perpendicular to $\hat{\mathbf{x}}$). For such cylinder, the general electromagnetic theory predicts that the external field is equivalent to that of a transversally oriented "line dipole" extending along the cylinder axis. Then, one may show that it is also equivalent to the field created by two parallel infinite lines of pole densities $\rho = \pm SM/\delta$ per unit length ($S = \pi R^2$ being the cylinder sectional area) separated by a distance δ along the transverse direction $\hat{\mathbf{t}} = \mathbf{M}/M$, in the limit $\delta \rightarrow 0$. Starting from the well-known expression of the scalar potential for such two lines, $V = 2|\rho|\log(r/r')$ with $\mathbf{r}' = \mathbf{r}' + \delta\hat{\mathbf{t}}$, and working out the limit $\delta \rightarrow 0$, as is done in reference [37], leads to the following expressions for the components of $\mathbf{h} = -\nabla V$ respectively parallel (radial component) and perpendicular to $\mathbf{r}$ (tangential component),

$$\mathbf{h_r} = 2\pi R^2 M \frac{\cos\omega}{r^2}\hat{\mathbf{e}}_\mathbf{r}, \quad \mathbf{h_n} = -2\pi R^2 M \frac{\sin\omega}{r^2}\hat{\mathbf{e}}_\mathbf{n} \tag{B.8}$$

where, referring to Figure 19b, ω is the angle between the magnetization $\mathbf{M}$ and the position vector $\mathbf{r}$ normal to the cylinder axis. From these relations, one can easily derive that the z component of the stray field and its second derivative with respect to z are respectively

$$h_z = 2\pi R^2 M\left[\frac{z^2-y^2}{\left(y^2+z^2\right)^2}\cos\varphi + \frac{2yz}{\left(y^2+z^2\right)^2}\sin\varphi\right] \tag{B.9}$$

and

$$\frac{\partial^2 h_z}{\partial z^2} = 12\pi R^2 M \times\left[\frac{y^4+z^4-6y^2z^2}{\left(y^2+z^2\right)^4}\cos\varphi + \frac{yz^3-y^3z}{\left(y^2+z^2\right)^4}\sin\varphi\right] \tag{B.10}$$

where φ is the angle between the cylinder magnetization $\mathbf{M}$ and the $\hat{\mathbf{z}}$ axis, φ being chosen as clockwise positive.

Appendix C: Role of the sample topography in the MFM imaging

The use of the tapping/lift^{TM} method for recording MFM images on samples having sharp topographical features, rather than a simpler method where the probing tip would fly along an horizontal trajectory (at constant z), may have in some cases major consequences on the observed magnetic contrasts. In order to illustrate this point, very important for the present study, and to demonstrate the role of the sample topography in the MFM imaging, a role often unrecognized, the MFM contrasts arising from an infinitely long wire with radius R and uniform transverse magnetization were simulated, using equations (B.2) and (B.10). For these simulations, the tip magnetization $\mathbf{m}$ was oriented along the $-\hat{\mathbf{z}}$ direction and the angle φ of the wire magnetization $\mathbf{M}$ was set to 90 degrees ($\mathbf{M} \parallel \hat{\mathbf{y}}$). Notice that, due to the infinite length of the magnetic cylinder, the calculated MFM contrasts are naturally invariant upon translation along the cylinder axis.

Figures 20b and 20c show respectively the MFM image and a densitometer trace along a line scan perpendicular to the cylinder axis computed in the case of an unrealistic "constant z" trajectory (Fig. 20a). Here, the MFM response mainly consists of two broad contrasts of opposite polarities which may be viewed as a mapping of the diametrically opposed negative and positive surface pole distributions associated with the transverse magnetization. However, as the tip was "numerically flown" at a fair distance above the cylinder, these contrasts naturally extend well beyond the region containing the cylinder ($-R \leq y \leq R$). If a more realistic probe trajectory is used in the computation (Fig. 20d), additional narrow peak contrasts may appear along the sides of the cylinder. This is clearly shown in Figures 20e and 20f which present results obtained in the case of a strongly non-rectilinear trajectory. This trajectory was built by convoluting the cylinder sectional shape with a tip-apex shape consisting of a vertically elongated half-ellipse and by translating vertically the resulting topographical profile by a certain amount, as is done in the tapping/lift^{TM} method. One trivial though valid argument to explain the substantial differences in the MFM contrasts calculated for the two kinds of tip trajectories (realistic and unrealistic) consists in saying that the stray field from the magnetized body

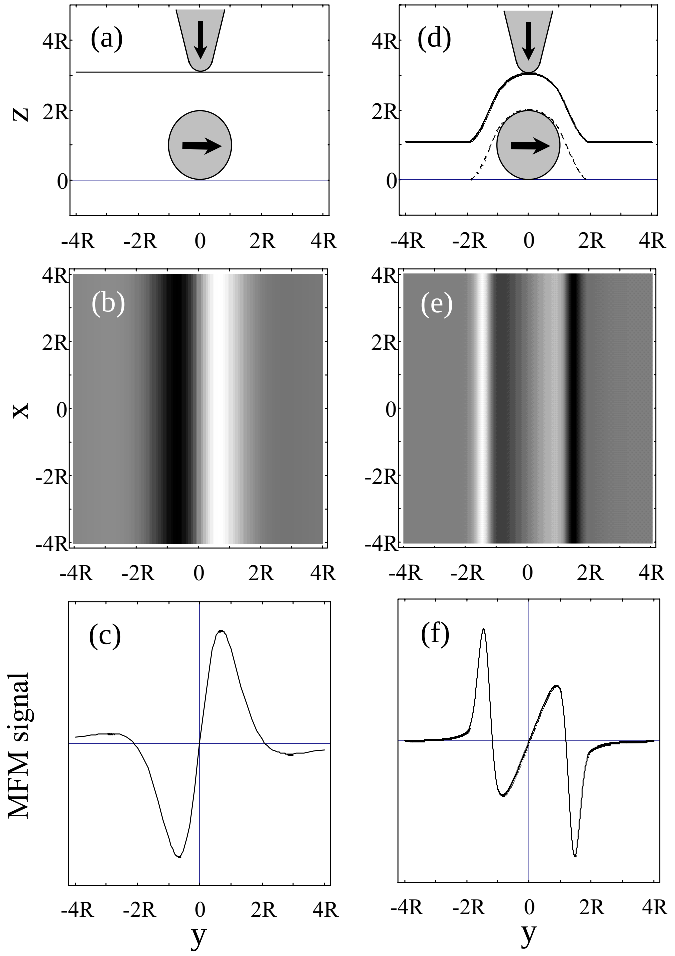

Fig. 20. (b, e) Theoretical MFM images and (c, f) contrast profiles along line scans perpendicular to the cylinder axis computed for an infinite transversally magnetized straight cylinder with radius R parallel to $\hat{\mathbf{x}}$ ($\mathbf{M} \parallel \hat{\mathbf{y}}$). Two kinds of tip trajectories were considered: (a–c) Unrealistic “constant z” trajectory, (d–f) realistic trajectory. The dashed line in (d) is the topographical profile from which the realistic tip trajectory was deduced by translation along $\hat{\mathbf{z}}$.

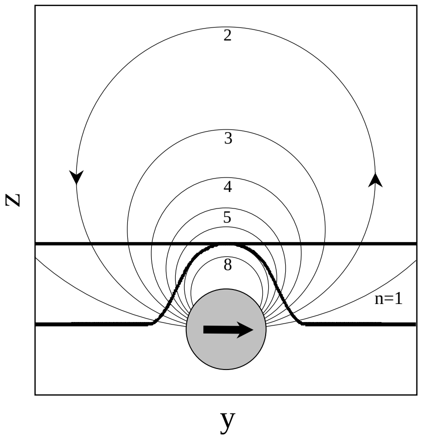

Fig. 21. Schematic of the stray field lines from an infinite transversally magnetized cylinder ($\mathbf{M} \parallel \hat{\mathbf{y}}$). These are circles tangential to the magnetization vector and having radii inversely proportional to n, n being integer. Also shown are the realistic and unrealistic tip trajectories considered in Figure 20 (thick solid lines).

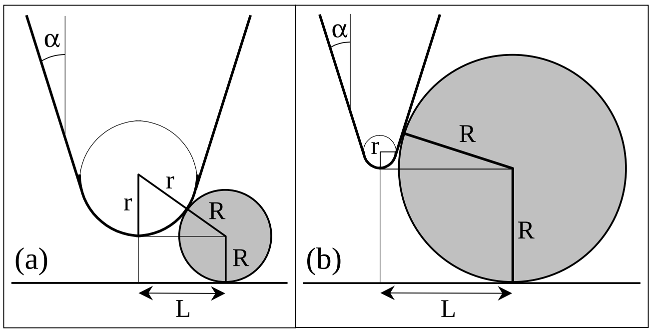

Fig. 22. Geometry considered to evaluate the effect of tip geometrical hindrance on the half-height width ($2L$) of the topographical section profiles measured by AFM on nanowires: (a) Ratio of wire (R) to tip apex (r) radii smaller than ($1/\sin\alpha - 1$), (b) R/r larger than ($1/\sin\alpha - 1$).

is not probed at the same locations in the two cases. Furthermore, these differences may be accounted for qualitatively by examining how the trajectories cross the stray field lines associated with the magnetized cylinder. For an infinite transversally magnetized cylindrical wire, the stray field lines are circles tangential to the magnetization vector [38], as sketched in Figure 21. As the tip is moved along a realistic trajectory and travels up or down the cylinder flanks, it is subjected to rapid changes in stray field, hence in magnetic force, as revealed by the large density of field lines that are crossed in the vicinity of the cylinder sides. Thus, strong MFM contrasts may be recorded, which are either absent or proportionally much less pronounced when the tip is flown along a rectilinear trajectory, not probing the stray field in a so tight manner around the cylinder. Notice that the occurrence of additional side contrasts is not restricted to the particular geometry chosen for our simulations ($\mathbf{M} \parallel \hat{\mathbf{y}}$). Although less pronounced as the angle φ tends towards zero ($\mathbf{M} \parallel \hat{\mathbf{z}}$), this effect may indeed occur whatever the angle of the cylinder magnetisation.

In conclusion, the interpretation of MFM contrasts recorded in the lift mode on samples having sharp topographical features may require to take into account the exact trajectory of the magnetic probe. Furthermore, in the presence of additional side contrasts, a MFM image may no longer be seen as a simple mapping of the magnetic charges in the sample.

Appendix D: Effect of the tip geometrical hindrance on the topographical profiles

The effect of tip geometrical hindrance, sketched in Figure 22, is intrinsic to most scanning force microscopy techniques. It may only be considered as negligible when the size of the probe is much smaller than that of the topographical features to be imaged. If this condition is not fulfilled, sharp features of the sample surface, as our nanowires, can act as imaging protrusions so that the topographical profiles reflect to a certain extent the shape of the probe rather than that of the samples [39]. Such a geometrical effect limiting the spatial resolution and giving rise to an apparent broadening of the sample features unavoidably occurs in the case of our nanowires since the curvature radii of the tips used are in the range of 30 to 50 nm (according to the manufacturer), that is comparable to the lateral size of the nanowires.

Assuming the simple tip-sample geometry outlined in Figure 22, an expression for the half-height width of the topographical profile may be obtained, which depends on the ratio of the wire ($R = \phi/2$) to tip apex (r) radii. If R/r is smaller than $(1/\sin\alpha - 1)$ (Fig. 22a), it is the hemispherical apex of the tip that is in "contact" with the sample when the tip is located at $y - y_c = \pm L$ (Fig. 22a). Then, $2L$ reads

$$2L = 2\sqrt{R^2 + 2rR}. \tag{D.1}$$

If, on the contrary, R/r is larger than $(1/\sin\alpha - 1)$ (Fig. 22b), it is one of the flat faces of the square-based pyramidal tip that is in "contact" with the wire (Fig. 22b) and $2L$ is given by

$$2L = 2\left[\frac{1+\tan^2(\alpha/2)}{1-\tan^2(\alpha/2)}\right] R + 2\left(\frac{1-\sin\alpha}{\cos\alpha}\right) r. \tag{D.2}$$

The intrinsic lateral broadening of the topographical profiles across the nanowires was estimated using these two equations. The shaded area in Figure 10e shows what the profile half-height width would be for $\alpha = 17°$ (manufacturer's data) and tip apex radii ranging between 30 to 50 nm if the tip geometrical hindrance were the only source of broadening. It is clear from Figure 10e that a significant part but not the whole broadening of the wire profiles may be attributed to intrinsic geometrical effects (see Sect. 5.1).

References

1. W. Wernsdorfer, B. Doudin, D. Mailly, K. Hasselbach, A. Benoit, J. Meier, J.-P. Ansermet, B. Barbara, Phys. Rev. Lett. **77**, 1873 (1996); W. Wernsdorfer, K. Hasselbach, A. Benoit, B. Barbara, B. Doudin, J. Meier, J.-P. Ansermet, D. Mailly, Phys. Rev. B. **55**, 11552 (1997).
2. A.O. Adeyeye, G. Lauhoff, J.A.C. Bland, C. Daboo, D.G. Hasko, H. Ahmed, Appl. Phys. Lett. **70**, 1046 (1997).
3. T. Ono, H. Miyajima, K. Shigeto, T. Shinjo, Appl. Phys. Lett. **72**, 1116 (1998).
4. J.-E. Wegrowe, D. Kelly, A. Franck, S.E. Gilbert, J.-P. Ansermet, Phys. Rev. Lett. **82**, 3681 (1999).
5. K.J. Kirk, J.N. Chapman, C.D.W. Wilkinson, J. Appl. Phys. **85**, 5237 (1999).
6. T. Hirayama, Q. Ru, T. Tanji, A. Tonomura, Appl. Phys. Lett. **63**, 418 (1993).
7. M. Lederman, S. Schultz, M. Ozaki, Phys. Rev. Lett. **73**, 1986 (1994).
8. M. Hehn, K. Ounadjela, J.-P. Bucher, F. Rousseaux, D. Decanini, B. Bartenlian, C. Chappert, Science **272**, 1782 (1996).
9. L. Belliard, J. Miltat, A. Thiaville, S. Dubois, J.-L. Duvail, L. Piraux, J. Magn. Magn. Mater. **190**, 1 (1998).
10. S.Y. Chou, Proc. IEEE, **85**, 652 (1997).
11. C.R. Martin, Adv. Mater. **3**, 457 (1991).
12. T.M. Whitney, J.S. Jiang, P.C. Pearson, C.L. Chien, Science **261**, 1316 (1993).
13. I. Chlebny, B. Doudin, J.-P. Ansermet, Nanostruct. Mater. **2**, 637 (1993).
14. E. Ferain, R. Legras, Nucl. Instrum. Meth. B **82**, 539 (1993); Nucl. Instrum. Meth. B **84**, 331 (1994); Nucl. Instrum. Meth. B **131**, 97 (1997).
15. I.M. Croll, IEEE Trans. Mag. **23**, 59 (1987).
16. L. Piraux, S. Dubois, E. Ferain, R. Legras, K. Ounadjela, J.-M. George, J.-L. Maurice, A. Fert, J. Magn. Magn. Mater. **165**, 352 (1997).
17. J.-L. Maurice, D. Imhoff, P. Etienne, O. Durand, S. Dubois, L. Piraux, J.-M. George, P. Galtier, A. Fert, J. Magn. Magn. Mater. **184**, 1 (1998).
18. D.M. Paige, B. Szpunar, B.K. Tanner, J. Magn. Magn. Mater. **44**, 239 (1984).
19. See for example, R.F. Pearson in *Experimental Magnetism* (John Wiley & Sons, New York, 1979), Vol. 1, pp. 183–185.
20. E.C. Stoner, E.P. Wohlfarth, Philos. Trans. London Ser. A **240**, 599 (1948).
21. P. Grütter, H.G. Mamin, D. Rugar, in *Scanning Tunneling Microscopy*, edited by R. Wiesendanger, H.-J. Güntherodt (Springer, Berlin 1992), Vol. II, pp. 151–207; and references therein.
22. A. Hubert, R. Schäfer, *Magnetic domains* (Springer, Berlin, 1998).
23. R. O'Barr, M. Lederman, S. Schultz, W. Xu, A. Scherer, R.J. Tonucci, J. Appl. Phys. **79**, 5303 (1996).
24. M. Hehn, S. Padovani, K. Ounadjela, J.-P. Bucher, Phys. Rev. B **54**, 3428 (1996).
25. U. Ebels, P.E. Wigen, K. Ounadjela, Europhys. Lett. **46**, 94 (1999).
26. U. Ebels, L. Buda (private communication).
27. J.P. Jakubovics, Philos. Mag. **14**, 881 (1966).
28. M. Hehn, Ph.D. Thesis, Louis Pasteur University of Strasbourg (1997).
29. M. Muller, J. Appl. Phys. **38**, 2413 (1967).
30. J.A. Cape, G.W. Lehman, J. Appl. Phys. **42**, 5732 (1971).
31. A. Wadas, J. Magn. Magn. Mater. **71**, 147 (1988); J. Magn. Magn. Mater. **72**, 295 (1988).
32. In these calculations, the demagnetizing energy is evaluated using the method given in pp. 122–124 of reference [22].
33. U. Ebels, A. Radulescu, Y. Henry, L. Piraux, K. Ounadjela, Phys. Rev. Lett. **84**, 983 (2000).
34. Q. Zhong, D. Inniss, K. Kjoller, V.B. Elings, Surf. Sci. **290**, L688 (1993).
35. See *e.g.* D. Craik, *Magnetism, Principles and Applications* (John Wiley & Sons, Chichester, 1995), p. 338.
36. There exists no analytical expression for the field emanating from a transversally magnetized cylinder with finite length. This is essentially due to the fact that there is no easy conversion of the integrals that arise in the calculation to elliptic integrals.
37. J. Granier, *Introduction à l'Étude des Champs Physiques* (Dunod, Paris, 1941), pp. 115–116.
38. E. Durand, *Magnétostatique* (Masson, Paris, 1968), pp. 54, 157.
39. See *e.g.* D. Keller, Surf. Sci. **253**, 353 (1991).